COMMUNICATION SCIENCES INSTITUTE

"Generation, Filtering, and Applications of Subcarriers in Optical Communication Systems"

by

Steven Arthur Havstad

CSI-00-12-03

USC VITERBI SCHOOL OF ENGINEERING
UNIVERSITY OF SOUTHERN CALIFORNIA
ELECTRICAL ENGINEERING — SYSTEMS
LOS ANGELES, CA 90089-2565

GENERATION, FILTERING, AND APPLICATIONS OF SUBCARRIERS IN OPTICAL COMMUNICATION SYSTEMS

by

Steven Arthur Havstad

A Dissertation Presented to the
FACULTY OF THE GRADUATE SCHOOL
UNIVERSITY OF SOUTHERN CALIFORNIA
in Partial Fulfillment of the
Requirements for the Degree
DOCTOR OF PHILOSOPHY
(ELECTRICAL ENGINEERING)

December 2000

DEDICATION

To my parents, Peter and Jeaneane Havstad, for fostering a lifelong interest in learning.

ACKNOWLEDGEMENTS

Any undertaking of this magnitude would not be possible without the assistance, encouragement, understanding, support, friendship, and love of a large number of people.

At Northrop, where it all began, Ed Knobbe got me started. Ed, this is all your fault.

At USC, the staff of the Communication Sciences Institute, especially Milly Montenegro, was invaluable.

My colleagues in the Optical Communications Lab, past and present. I have no doubt that this is the best research group anywhere.

Baruch Fischer, for a treasured friendship, some great ideas, and lots of help, encouragement, and inspiration.

The boss, Alan Willner, for taking a chance on an old man and providing a wonderful opportunity to learn all about optical fiber communications. I am happy to leave, but I will always be thankful for the time I spent in your lab.

Finally, my wife Susan, I couldn't have done this without you. This was as much work for you as it was for me. A guy couldn't ask for a more supportive wife.

CONTENTS

LIST OF FIGURES

ABSTRACT

GENERATION, FILTERING, AND APPLICATIONS OF SUBCARRIERS IN OPTICAL COMMUNICATION SYSTEMS

I investigate several novel aspects of subcarriers in optical communication systems, including generation, filtering, and applications such as synchronization, contention resolution, and tunable dispersion compensation.

Low-biased modulation is attractive but inefficient. I develop an optically-efficient RF modulator that uses a novel arrangement of two low-biased Mach-Zehnder modulators within a ring laser. By recirculating the unused output of the first modulator, I improve optical efficiency by over seven dB.

Laser sources for optical heterodyning must have high spectral purity and be tunable. Using a delayed self-heterodyne interferometer and narrow-linewidth fiber laser, I study the evolution of the interferometer output with increasing fiber delay. I demonstrate the importance of a long fiber delay and a Voigt fit to the output to determine the true fundamental linewidth. I also demonstrate a stable narrow-linewidth single-mode erbium-doped fiber ring laser with a 40-nm tuning range of 1522-1562 nm. I achieve wide tunability using a highly-stretchable FBG, representing a 3.5-fold increase in tuning range over prior art using FBGs.

Subcarrier filtering in the optical domain avoids electronic processing bottlenecks and costly optical-to-electrical-to-optical conversions. I present a novel all-fiber narrowband notch or bandpass filter based on pump-induced saturable gain or absorber gratings in a loop mirror. The loop-mirror filter has potential bandwidths from the sub-MHz to beyond the GHz regimes, and is optically tunable.

Fast and efficient routing, multiplexing, and contention resolution requires incoming bit streams to be synchronized before entering a network switching node. I demonstrate bit synchronization of two NRZ input signals to within 1/8 of a bit time using a subcarrier for determining the time delay between two baseband channels.

Contention resolution without optical buffering or deflection routing can reduce network traffic delays. I demonstrate an optical contention resolution technique that combines two identical-wavelength contending 2.5 Gb/s channels into the same output-port wavelength channel.

Dispersion can cause serious power fading in subcarrier-multiplexed transmission. I use a tunable nonlinearly-chirped FBG in a phase diversity configuration to achieve distance-independent microwave and millimeter-wave power fading compensation for DSB subcarrier-multiplexed systems.

1. Introduction

Optical communication systems have revolutionized the world. The development of high bandwidth low loss optical fiber (see Figure 1) coupled with the advent of the erbium-doped optical amplifier has led to the proliferation of the Internet and a host of new multi-billion dollar industries. Yet, demand for bandwidth continues to increase exponentially, and although techniques such as wavelength-division multiplexing promise a solution, novel solutions to a myriad of technical challenges continue to be required to satisfy this ever-increasing need. Despite the fact that current fiber-based optical communication systems use digital on-off modulation, analog subcarriers can be used successfully in such systems to provide solutions to some of the problems that must be resolved in order to realize next-generation high-capacity, reconfigurable optical systems and networks.

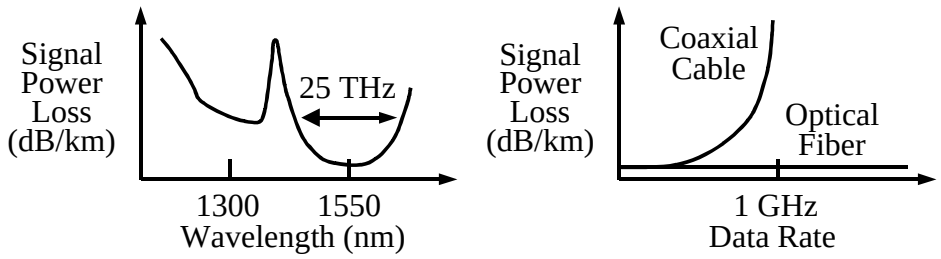

Figure 1. Optical fiber has the advantages of high bandwidth and low loss.

My research has focused on several novel aspects of using subcarriers in optical communication systems, including (i) the generation of subcarriers, by either external modulation or optical heterodyning, (ii) narrowband tunable optical filters for routing or processing subcarriers, and (iii) applications which use subcarriers, such as synchronization, contention resolution, and tunable dispersion compensation.

One attractive external modulation technique is low-biased modulation. Low-biased Mach-Zehnder modulation provides increased linear dynamic range, but is inherently inefficient because most of the optical power is lost. We have developed an optically-efficient RF modulator

that uses a novel arrangement of two low-biased Mach-Zehnder modulators within a ring laser [23]. The dual Mach-Zehnder modulators eliminate resonances due to the relaxation oscillation and laser cavity modes allowing operation over a wide bandwidth. This configuration also preserves the modulator transfer function and provides single-frequency output. In addition, by recirculating the unused output of the first Mach-Zehnder modulator, optical efficiency is improved by over seven dB relative to a similar externally-modulated configuration. This technique may be useful in analog photonic links when available dc power is limited.

In optical heterodyning, two lasers are mixed to generate a beat signal at a frequency corresponding to the wavelength difference between the laser outputs. These lasers each must have a high spectral purity, and should be tunable. Using a delayed self-heterodyne interferometer and a narrow-linewidth fiber laser, we study the evolution of the interferometer output beat signal with increasing fiber delay [24]. We demonstrate the importance of a long fiber delay and a Voigt fit to the interferometer output data to determine the true fundamental linewidth of a narrow-linewidth fiber laser. For our laser, we measure a Lorentzian linewidth of 750 Hz for fiber delays greater than 70 km. We also demonstrate a stable narrow-linewidth single-mode erbium-doped fiber ring laser with a 40-nm tuning range of 1522-1562 nm [51]. The wide tunability is achieved using a highly-stretchable fiber Bragg grating that exhibits a filter tuning range of over 50 nm. This represents a 3.5-fold increase in wavelength tuning range over prior art using FBGs.

Filtering of subcarriers should be done in the optical domain to avoid electronic processing bottlenecks and costly optical-to-electrical-optical conversions. We present a novel all-fiber narrowband filter based on pump-induced saturable gain or absorber gratings in a loop mirror [22]. Our design provides built-in interferometric phase alignment of the signal to the grating for optimal filtering. Notch or bandpass functionality is determined by the choice of gain or absorption and the input ports selected for the pump and signal. The loop-mirror filter has potential bandwidths from the sub-MHz to beyond the GHz regimes, and is optically tunable by

changing the wavelength of the pump light that establishes the grating. Such filters have potential applications to wavelength-division multiplexed optical networks and optical RF signal processing.

Fast and efficient routing, multiplexing, and contention resolution requires the incoming bit streams be synchronized before entering a network switching node. We demonstrate bit synchronization of two 1-Gb/s NRZ input signals to within 125 ps (1/8 of a bit time) using a subcarrier as the control signal for determining the time delay between the two baseband channels [47]. The 1-GHz subcarrier for each channel is superimposed onto the baseband data at the transmitter, then recovered and mixed in real time with a local clock at the switching node to generate a signal proportional to the relative phase differential. This phase differential signal is used to dynamically set optical space switches thereby controlling the path through a matrix of delay lines. Each channel is independently synchronized to the local clock, resulting in the synchronization of the two output streams to within a fraction of a bit time.

Contention resolution without optical buffering or deflection routing can reduce network traffic delays. We demonstrate an optical contention resolution technique that combines two identical-wavelength contending 2.5 Gb/s channels into the same output-port wavelength channel [2]. This is achieved by optically upconverting one channel to a higher microwave frequency beyond the other channel's baseband signal and routing both channels out the desired output-port wavelength channel simultaneously. By using narrow (~5 GHz) fiber Fabry-Perot filters for optically demultiplexing the two channels, we recover each channel using a baseband receiver with <1 dB power penalty.

Dispersion can cause serious power fading in subcarrier-multiplexed transmission. We use a nonlinearly-chirped FBG in a phase diversity configuration to achieve distance-independent power fading compensation for DSB subcarrier-multiplexed systems [21]. We demonstrate

compensation for dispersion-induced power fading from 0 to 150 km at 8 and 12 GHz, with received subcarrier power in all cases uniform to within 1 dB.

2. Generation of Subcarriers

2.1 An Optically-Efficient RF Modulator

Fiber-optic links offer many well known advantages relative to coaxial cables in terms of size, weight, loss, bandwidth, security, susceptibility to electromagnetic interference, and compatibility with high-speed optical signal processing techniques. In analog photonic links, carrier suppression by low-biased Mach-Zehnder modulation of optical signals at the transmitter provides the additional advantages of superior linear dynamic range, improved noise figure, and increased spur-free dynamic range [1, 12, 31]. Low-biasing, however, is inherently inefficient because most of the optical power is wasted. It is typically assumed that the decreased throughput of the modulator due to low-biased operation can be overcome simply by increasing the optical power input to the modulator [11, 12, 31]. However, in situations where the transmitter is dc-power limited, such as space-based applications, this approach may not be feasible, and it is essential to improve the efficiency of the transmitter. We have developed an optically-efficient RF modulator (OERFM) that recirculates the complementary portion of the low-biased output, resulting in an efficiency improvement of more than seven dB relative to a similar, externally-modulated laser.

The experimental configuration of OERFM is shown in Figure 2. The first Mach-Zehnder modulator is dc-biased at 5% transmission (our modulator low-bias point) to provide the OERFM output. The complementary 95% output is connected to a second Mach-Zehnder modulator, also dc-biased at 5% transmission, but at the opposite slope along the modulator transfer function. The 95% output of this second modulator is then recirculated through the ring laser. The second modulator cancels the modulation imposed on the recirculating light due to the first modulator. This cancellation is effected by applying a delayed, attenuated copy of the first modulator's RF drive signal to the second Mach-Zehnder modulator. Since the second modulator is operated at the same bias point as the first modulator, but on the inverse portion of the second modulator's

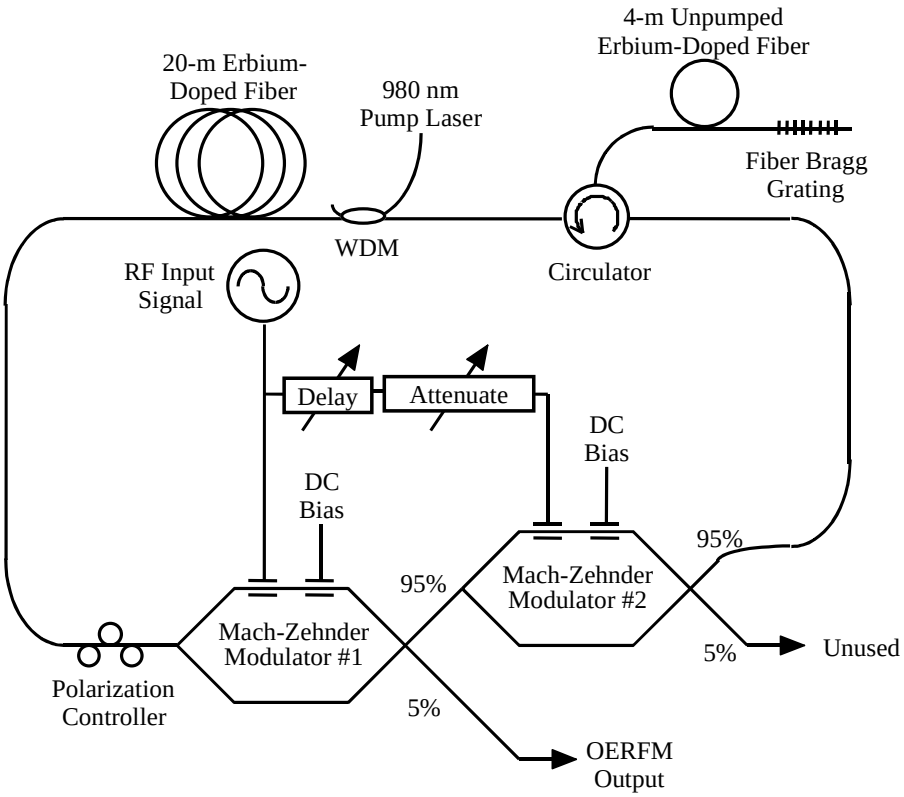

Figure 2. OERFM experimental configuration.

transfer function, the second modulator removes the modulation applied to the recirculating signal by the first modulator. Thus, the pair of modulators appears to the ring to be a constant, fixed loss. The bias set-points of both modulators are maintained by a simple bias-control circuit, using 1% of the light tapped off from each pair of modulator outputs (not shown). An optical circulator and fiber Bragg grating (0.3-nm bandwidth) provide unidirectional operation of the ring and wavelength selectivity. An unpumped 4-m section of erbium-doped fiber is also included between the circulator and the fiber Bragg grating. The standing wave created in this saturable absorber by reflection off the fiber Bragg grating forms an additional weak narrowband filter [5, 27]. This "smart" filter is adaptive, tracking slow frequency variations of the cavity modes and further suppressing the cavity modes of the ring, forcing single-frequency operation. Gain is provided by 20 m of erbium-doped fiber, pumped at 980 nm.

OERFM is operated with its amplifier in saturation. Since most of the light is recirculated through the ring by the low-biased modulator, the input to the modulator is relatively constant and the modulator transfer function is preserved. Figure 3 shows the transfer function of OERFM as a function of applied dc bias voltage. Note that the agreement with the theoretical transfer function is good near our 5% low-bias points. The transfer function begins to diverge near quadrature as more light is coupled out of the ring.

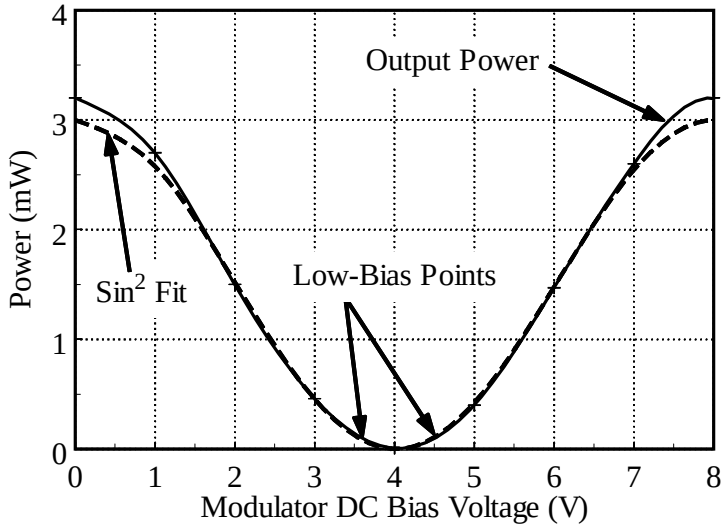

Figure 3. Measured OERFM transfer function plotted against a theoretical $\sin^2(\cdot)$ fit.

Due to its ring structure, OERFM is susceptible to resonances due to RF drive frequencies at the relaxation oscillation frequency of the laser or at frequencies corresponding to cavity mode harmonics. For erbium-doped fiber lasers, the relaxation oscillation frequency is small, typically less than 1 MHz. The cavity mode spacing in our experiment was about 5 MHz. However, proper adjustment of the timing and attenuation of the RF drive signal to the second modulator damps out both of these types of resonances. Figure 4 shows the effectiveness of the cancellation due to the second modulator as the RF drive frequency is scanned across a strong resonance (cavity mode) at about 89.05 MHz. Note that when the RF drive signal to the second modulator is over-attenuated, there is an enhanced response at the resonant frequency. Conversely,

when the drive signal to the second modulator is under-attenuated, the second modulator is overcompensating for the perturbation induced by the first modulator, resulting in a dip in the response at the resonant frequency. Only when both the timing and attenuation are set properly does the second modulator cancel the modulation applied to the first modulator completely.

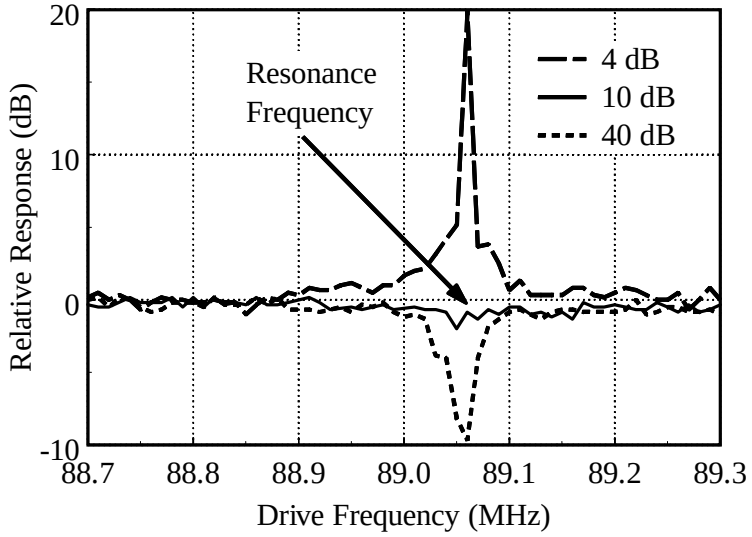

Figure 4. Output response of OERFM as a function of RF input frequency for three different attenuations to the second modulator. When the attenuation of the RF signal to the second modulator is set to 10 dB, the perturbation induced in the ring by the first modulator is perfectly canceled.

To measure the improvement in efficiency of OERFM, we compared the output power to an externally-modulated configuration, shown in Figure 5, as a function of diode pump current. OERFM demonstrates over 7-dB improvement in efficiency relative to the externally-modulated transmitter at 53 mW of pump power. The externally-modulated transmitter was spliced, so by splicing OERFM, we could increase this efficiency improvement by perhaps another dB. In addition, by integrating both modulators in a single chip, cavity loss could be reduced by several more dB, further improving our efficiency.

Single-frequency operation was verified using a Fabry-Perot optical spectrum analyzer with a resolution of 1.2 MHz. Note that when the unpumped erbium-doped fiber (EDF) was

removed and replaced by just a fiber Bragg grating, the optical spectrum analyzer indicated multimode operation with frequent mode hopping, demonstrating the effectiveness of the filter induced in the unpumped EDF. In addition, the linewidth was measured using the self-heterodyne technique with a 26.7-km fiber delay. The results of this measurement are shown in Figure 6, indicating a linewidth of approximately 1.5 kHz. A more detailed investigation of the linewidth of a similar laser is given in Section 2.2.1.

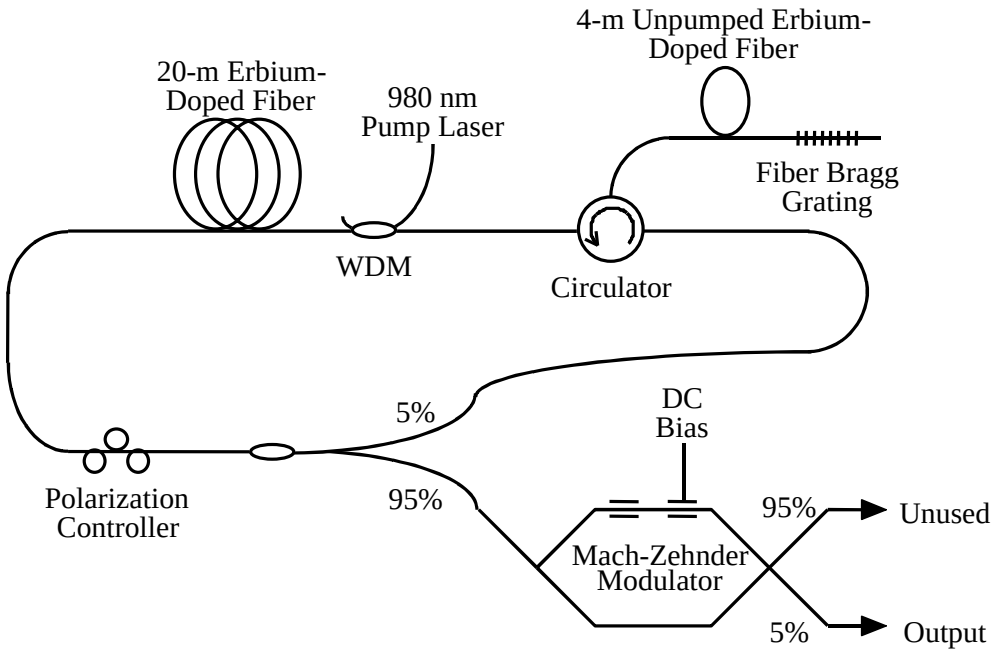

Figure 5. The efficiency improvement of OERFM was calculated by comparison to this externally-modulated configuration.

The measured relative intensity noise of OERFM was better than -149 dB/Hz, which was the limit of our measurement equipment.

With only a single modulator in the ring, the narrowband filter induced in the unpumped section of EDF was not strong enough to prevent resonance when the modulator was driven at an RF frequency corresponding to one of the cavity modes of the ring. It is possible that by experimenting with other lengths of unpumped EDF with different erbium concentrations, the

filter bandwidth and strength characteristics could be changed to allow operation of a single-modulator design across cavity modes without resonance. It might also be advantageous to operate the EDFA closer to the onset of saturation, lowering the gain slightly to further discourage unwanted modes from lasing.

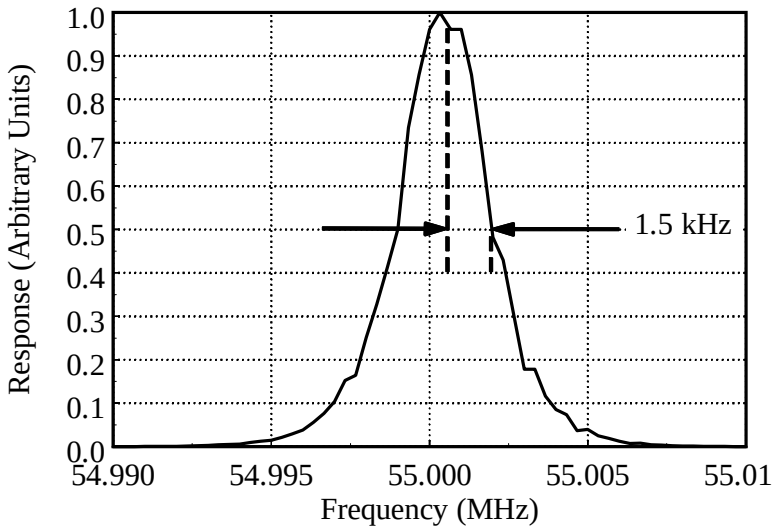

Figure 6. Self-heterodyne laser linewidth measurement, 26.7-km delay line.

Further improvements are possible with a monolithic semiconductor implementation of OERFM. Obviously, the physical size of this device would be much smaller than our current configuration. Also important is the fact that the semiconductor optical amplifier can be pumped electrically, eliminating the optical-to-optical conversion stage in the EDFA, resulting in much higher wall-plug efficiency. Since resonances are eliminated using the OERFM dual-modulator configuration, operation is possible even in the region of the relaxation resonance frequency, which is not as easy to avoid in semiconductor lasers as in erbium-doped fiber ring lasers.

We have demonstrated a technique to improve the dc power efficiency of a low-biased Mach-Zehnder modulator by over 7 dB. By using a ring laser to recirculate the optical power that is normally wasted, we provide single-frequency output while preserving the modulator transfer function. This concept should make low-biased operation of Mach-Zehnder modulators more

attractive, especially for applications where available dc power is limited such as in space-based systems.

2.2 Heterodyning of Narrow-Linewidth Lasers

High frequency millimeter-wave signals can be generated by mixing two optical carriers whose frequencies differ by the desired frequency [54]. This technique is attractive because it avoids bandwidth limitations of existing external modulators and drivers, but imposes stringent requirements on the linewidth and tunability of the lasers used to generate these signals.

2.2.1 Delayed Self-Heterodyne Interferometer Measurements of a Narrow-Linewidth Fiber Laser

Narrow-linewidth lasers are important for many applications, including spectroscopy, optical heterodyning, coherent communications, and sensing. One key practical technology for generating narrow linewidths is the fiber ring laser. When operated in a single longitudinal mode, fiber ring lasers can routinely exhibit linewidths of several kHz, due to their characteristically long cavity lengths.

The standard tool for high-resolution linewidth measurements of narrow-linewidth lasers is the delayed self-heterodyne interferometer (DSHI), in which one path is delayed to decorrelate the phases of the optical fields before recombination. Unfortunately, the results of this tool are often interpreted incorrectly due to a misunderstanding of the resultant power spectrum.

Since the introduction of the DSHI in 1980 [38], much work has been done to understand the theory underlying the operation of this tool. In 1986, a theoretical model was developed that predicted how the shape of the power spectrum evolves with increasing delay [44]. In 1991, linewidth broadening due to 1/f frequency noise was measured, and several techniques were proposed to isolate the critical Lorentzian component of the lineshape [37]. In 1992, the feasibility of using long fiber delays was demonstrated for increased measurement resolution, while

broadening due to optical amplifier noise was found to be negligible [8]. However, despite these contributions, many papers continue to be published in which short interferometer fiber delays are used and the interferometer output spectrum is misinterpreted, resulting in erroneous linewidth measurements. A proper analysis of the measured linewidth evolution, even using relatively short delays, can indirectly provide the linewidth, but single-point measurements are commonly in error. The most common error is to use a delay of only one or two times the laser's coherence length, and subsequently assume the resulting beat signal is Lorentzian, calculating the linewidth as one-half of the 3-dB bandwidth.

Using a delayed self-heterodyne interferometer and a narrow-linewidth erbium-doped fiber laser, we study the evolution of the interferometer output beat signal with increasing fiber delay. We demonstrate the importance of a long interferometer fiber delay and a Voigt fit to the interferometer output data to determine the true fundamental linewidth of a narrow-linewidth fiber laser. For our laser using a Voigt fit, we measure a Lorentzian linewidth of 750 Hz for delays from 70 to 190 km.

The configuration of the DSHI is shown in Figure 7. Our source was an erbium-doped fiber ring laser constructed in our lab [51], which is discussed in more detail in Section 0. This laser had a cavity length of 35.6 m, resulting in a cavity mode spacing of 5.6 MHz. The output power was set to –5 dBm at 1532 nm. Stable single-mode operation was provided using unpumped erbium-doped fiber as an intracavity saturable absorber [27], and verified using a Fabry-Perot optical spectrum analyzer with a free spectral range of 6 GHz and a resolution of 1 MHz. The fundamental linewidth of this laser was measured to be 750 Hz (corresponding to a coherence length of 85 km), using a Voigt fit with interferometer fiber delays from 70 to 190 km.

For semiconductor lasers with linewidths on the order of 1 MHz, it is easy to obtain delays that are many times the coherence length of the laser using less than a kilometer of fiber.

Fiber lasers, on the other hand, may have linewidths on the order of a kHz, and corresponding coherence lengths between 10 and 100 km. Based on our observations, as shown in Figure 8, the fiber ring laser appears to converge to a quasi-Lorentzian lineshape for a delay of about 100 km, as indicated by the lack of structure, or oscillations, in the low-power wings of the electrical power spectrum.

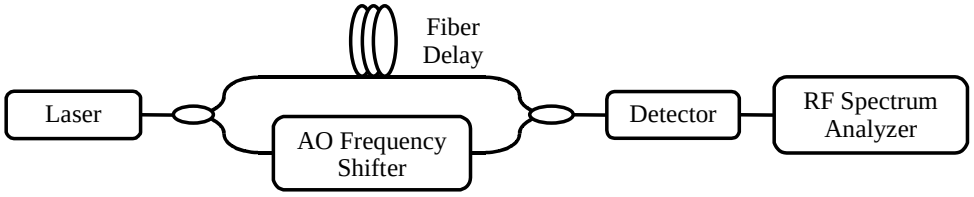

Figure 7. The delayed self-heterodyne interferometer.

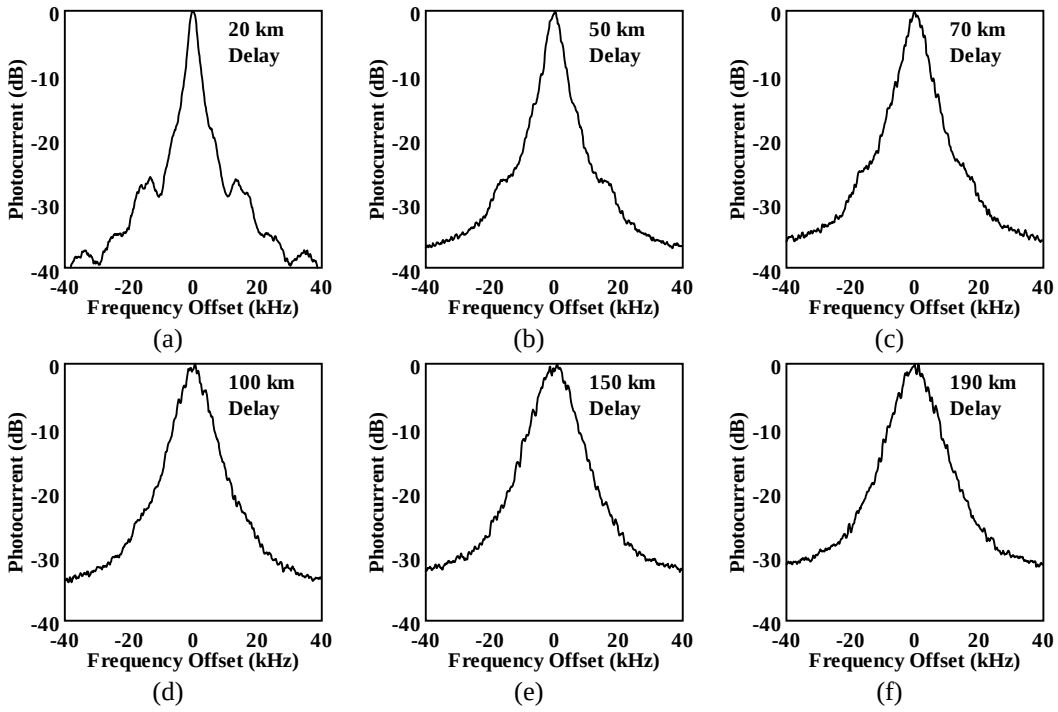

Figure 8. Evolution of the beat signal to a quasi-Lorentzian shape with increasing delay: (a) 20 km delay, (b) 50 km delay, (c) 70 km delay, (d) 100 km delay, (e) 150 km delay, (f) 190 km delay.

However, observation of this beat signal is often limited to the peak of the spectrum or with the display scale of the RF spectrum analyzer set to linear rather than logarithmic, in order to determine the 3-dB linewidth with the assumption of a Lorentzian lineshape. In these cases it is easy to overlook the structure that indicates coherent effects. In addition, a closer analysis of the evolution of the lineshape indicates that the linewidth includes a component that increases with increasing delay. This delay-dependent broadening is caused by 1/f noise, which includes low frequency components that remain correlated even with very long fiber delays [37]. Figure 9 shows measured 3-dB linewidths based on the peaks of the power spectra shown in Figure 8 and under the assumption of a Lorentzian lineshape. Figure 9(a) shows the peaks of the power spectra, and Figure 9(b) shows how the resulting 3-dB linewidth increases with increasing interferometer fiber delay. Because this technique overestimates the linewidth, it also gives a coherence length estimate that is too small. For a Lorentzian lineshape, measuring further down the power spectrum, i.e., at the -10, -20, and -30 dB power levels, can reduce the effects of frequency jitter [9]. However, as Figure 9(b) also shows, although the effects of the delay-dependent broadening are reduced, the measured linewidths in these cases still increase with increasing interferometer fiber delay.

The Lorentzian component of linewidth is proportional to phase noise, so for many applications it is important to isolate this Lorentzian component of the linewidth from the delay-dependent broadening [37]. The Voigt profile is commonly used to study spectral line shapes resulting from a superposition of independent Lorentzian and Doppler (Gaussian) line broadening mechanisms. The Voigt profile results from the convolution of a Lorentzian (homogeneous, white frequency noise) and a Gaussian (inhomogeneous, 1/f noise), and so a proper fit separates the Lorentzian linewidth component from the delay-dependent Gaussian linewidth component. Figure 10 compares Gaussian, Lorentzian, and Voigt fits to the measured interferometer output using a 70-km fiber delay. All fits were done using the shareware program GFit, version 9.1 [10].

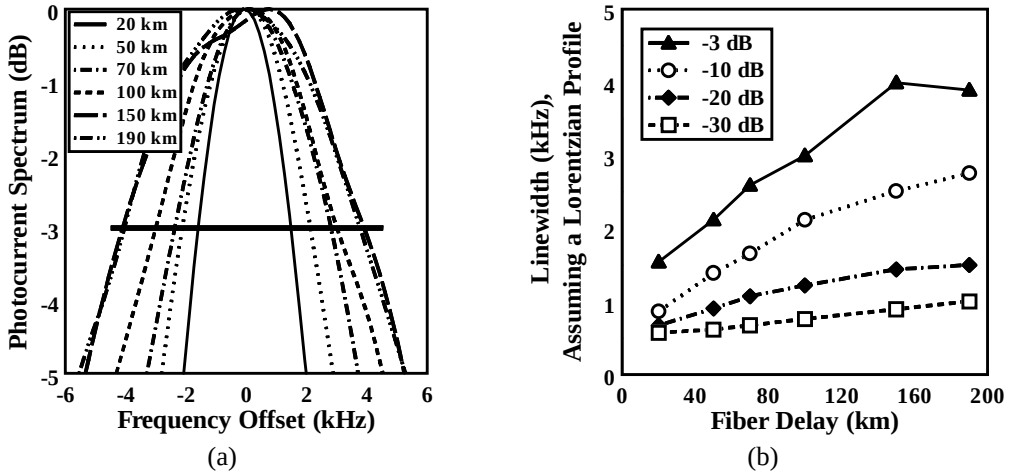

(a) (b)

Figure 9. (a) Evolution of the peak of the power spectra. (b) Assuming a Lorentzian line shape, the 3-dB linewidth as well as the 10-, 20-, and 30-dB linewidths all increase with increasing fiber delay.

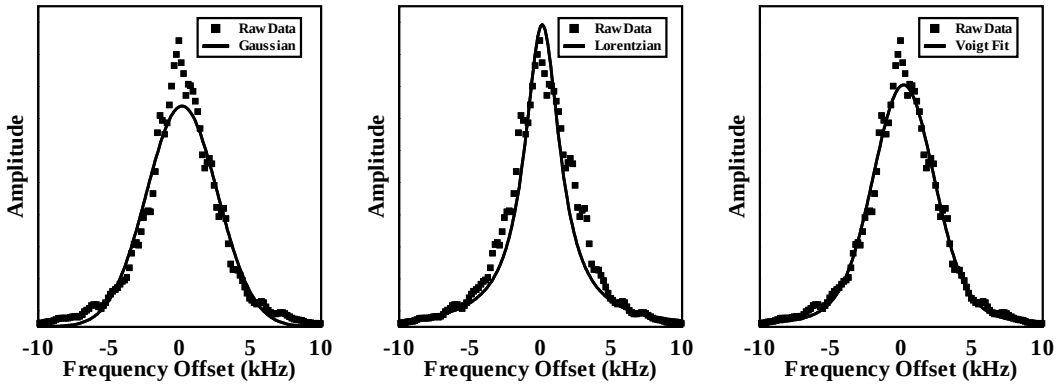

(a) (b) (c)

Figure 10. Comparison of (a) Gaussian, (b) Lorentzian, and (c) Voigt fits to the measured interferometer output using a 70-km fiber delay.

Both the Gaussian and Lorentzian profiles are relatively poor approximations to the measured data—the Gaussian does not fit the peak well and overestimates the lower power wings of the spectrum, while the Lorentzian is a good match to the peak but underestimates the width of the rest of the spectrum. The Voigt fit gives the best overall approximation to the measured lineshape. Figure 11 shows the results of the Voigt fit with the separate Gaussian and Lorentzian

components. The Gaussian component increases with increasing interferometer fiber delay length, but the Lorentzian component increases to 750 Hz at 70 km and then levels off all the way to 190 km. The Lorentzian component of a Voigt fit gives an accurate linewidth measure for delays greater than and approximately equal to the laser coherence length (85 km).

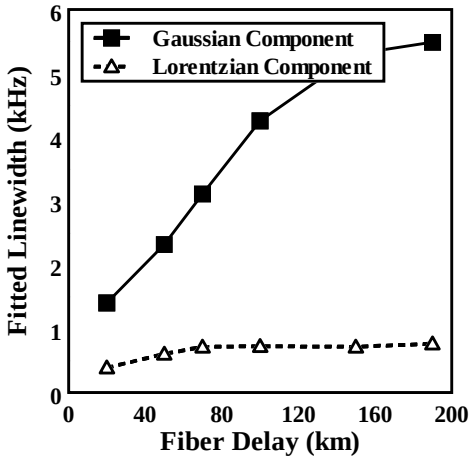

Figure 11. Gaussian and Lorentzian components of linewidth from Voigt fit.

2.2.2 A Single-Mode Erbium-Doped Fiber Ring Laser with 40-nm Tuning Range Using a Stretchable FBG

Fiber ring lasers have many attractive features including (i) narrow linewidths for system diagnostics and coherent applications, and (ii) easy wavelength tunability for testing of wavelength-division multiplexed (WDM) optical technologies. In order to provide full laser inventory reduction for WDM systems, such lasers should also have a wide tuning range. In general, tuning an intracavity optical filter can vary the wavelength of a fiber ring laser. Recent reports of fiber ring laser tunability have included the use of fiber Fabry-Perot filters [58], and free-space wavelength-selective gratings [43]. However, it would be desirable to use fiber Bragg gratings (FBGs) as the wavelength-selective intracavity element due to their advantages of fiber compatibility, ease of use, and low cost. Unfortunately, the fiber ring laser tuning range based on

the stretching of a FBG has been limited to ~11 nm [39] due to the relatively low mechanical strength of FBGs fabricated with the conventional processes of pulsed ultraviolet exposure and mechanical stripping.

We demonstrate a stable narrow-linewidth single-mode erbium-doped fiber ring laser with a 40-nm tuning range of 1522 to 1562 nm. Furthermore, the laser output power is constant with tuning. The wide tunability is achieved using a FBG with preserved mechanical strength that is capable of a filter tuning range of over 55 nm. We note that our technique using widely-tunable FBGs can be extended to include L-band fiber ring lasers to provide a significantly wider operational wavelength range.

Figure 12 shows the schematic of the fiber ring laser, which is simply the OERFM configuration discussed in Section 2.1 without the intracavity modulators. For narrow-linewidth operation and stable single-mode output, a 4-m section of unpumped erbium-doped fiber (EDF) is used as a saturable absorber in the cavity [5]. The unpumped EDF is coupled to the cavity by a circulator, which also acts as an isolator to provide unidirectional operation. A widely-tunable FBG is spliced to the saturable absorber and is tuned by simple stretching using a single mechanical stretching element. The active region of the laser consists of 20 m of EDF pumped with 980-nm light. Cavity outcoupling fractions from 5% to 95% of the intracavity light all exhibited similar stable operation with proper pump-level adjustment. All connections are either fusion spliced or FC/APC connectors. The total cavity length was 35.7 m, which resulted in a 5.6-MHz cavity mode spacing.

The FBG fabrication process, which preserves the mechanical strength of the fiber for enduring high amounts of stretching, is as follows. The acrylic jacket is removed in a hot (>200°C) sulfuric acid bath and the fiber is subsequently cleaned with acetone. The FBG is then written in this chemically-stripped deuterium-loaded fiber using UV light at 244 nm. Finally, the

fiber is recoated and annealed [32, 54]. The resulting FBG has 99% reflectivity, a 1522-nm center wavelength, and a 0.3-nm 3-dB bandwidth. By preserving the mechanical strength of the fiber, the FBG has a safe tuning range of over 50 nm, which encompasses the entire EDF gain spectral region (see Figure 13).

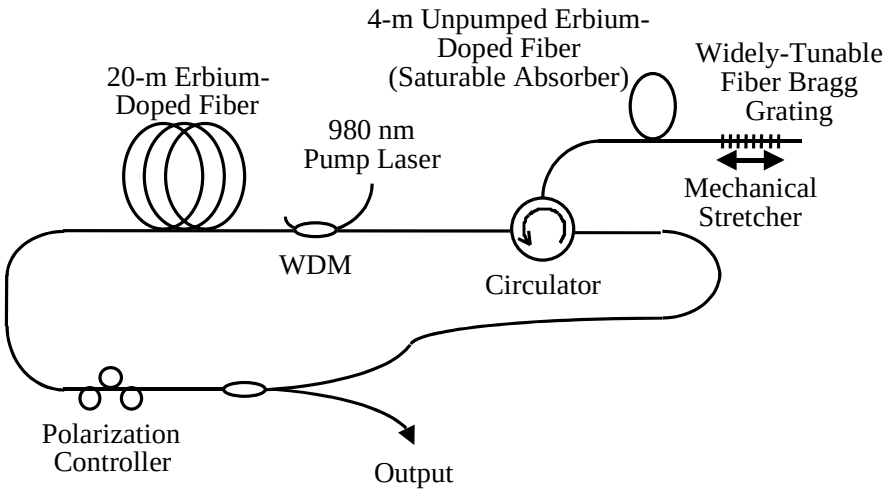

Figure 12. Configuration of our fiber ring laser using a widely-tunable FBG along with a saturable absorber to provide stable, single-mode operation.

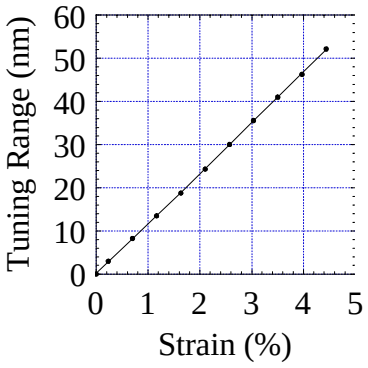

Figure 13. Measured tuning range of our widely-tunable FBG.

At the unstretched FBG center wavelength of 1522 nm, the laser threshold is observed at ~38 mW of pump power and the slope efficiency is 20% using a 3-dB outcoupler. For outcoupling

fractions of 20%, 10% and 5%, the slope efficiencies are 7%, 3.5%, and 2%. We verified single-mode operation using a scanning Fabry-Perot interferometer with a 6-GHz free spectral range and 1-MHz resolution. Figure 14 shows oscilloscope traces corresponding to (a) one free spectral range and (b) a single lasing mode. The cavity mode spacing of our laser was 5.6 MHz, but modes adjacent to the lasing mode were completely suppressed, as shown in the Figure 14(b).

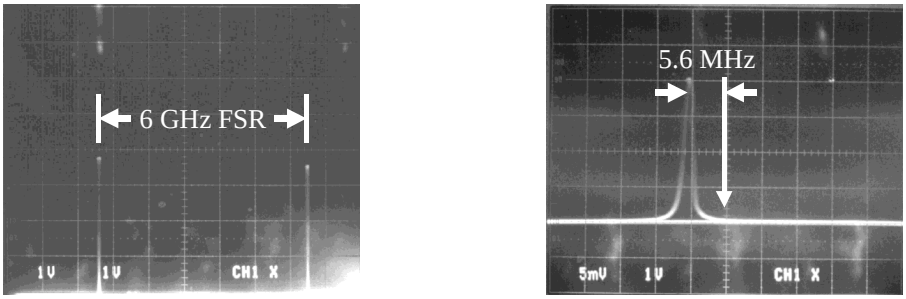

(a) (b)

Figure 14. Single-mode output spectrum for (a) a 6 GHz FSR corresponding to 6 V and (b) a magnified horizontal axis showing a single mode (5 mV/division).

The grating combined with the unpumped EDF provides lasing mode selection. Counterpropagating beams in the unpumped EDF form a standing wave that results in periodic spatial hole burning [5]. This creates a long absorption grating that results in a narrow bandwidth intracavity filter. The laser linewidth is measured to be 750 Hz, using the delayed self-heterodyne technique with a 150-km delay and a Voigt fit to extract the Lorentzian component [24] (see Section 2.2.1 for details).

Our 40-nm tuning range is achieved by simple mechanical stretching of the recoated FBG. This range covers the entire EDFA gain bandwidth, demonstrating the advantages of using widely-tunable elements for WDM systems. As the lasing wavelength is tuned, there is no distortion of the spectrum and output power is relatively constant (see Figure 15). Note that no gain-flattening filters were used to achieve our tuning range. Although our grating is capable of being safely tuned over a 50-nm range, we were unable to sustain lasing past 1562 nm. However, a

similar laser architecture should be able to provide tunable operation over the entire L-band as well.

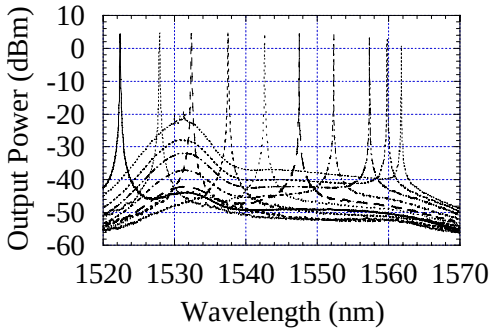

Figure 15. Spectra of shifted laser output peaks with a 5% outcoupling fraction.

3. Filtering of Subcarriers

3.1 Tunable Narrowband Notch or Bandpass Loop-Mirror Filters based on Saturable Gain or Absorber Gratings

Tunable narrowband optical filters are becoming increasingly important for a variety of different applications, such as supporting large numbers of closely spaced channels in dense wavelength-division multiplexed optical networks. Additionally, narrowband optical filters are useful for manipulating individual subcarrier-multiplexed channels within the optical domain, and in photonic links that engage in high-speed optical RF signal processing or that require tunable narrowband RF receivers. Common filter technology available for such applications includes arrayed waveguide gratings, thin-film dielectric interference filters, conventional fiber Bragg gratings, and fiber Fabry-Perot filters [45]. However, these options have difficulty providing either notch or bandpass filters with bandwidths less than 1 GHz. These approaches also suffer from one or more of the following disadvantages: (i) operation only at fixed wavelengths or over a limited range, (ii) requirement for mechanical or temperature tuning and temperature sensitivity, (iii) nonfiber design and large insertion loss, and (iv) periodic passbands.

Experiments were performed previously using erbium-doped fiber (EDF) as a saturable medium in a non-loop-mirror design to create simple light-induced Bragg reflection filters, but these filters did not account for the phase relationship between the signal and the pump-induced grating [14, 15, 17]. However, bandpass filters based on saturable absorber gratings have been shown to be effective for laser linewidth narrowing [5, 25, 26, 27]. More recently, self-filtering of signals [13] and fiber-laser frequency control [30] have also been demonstrated by use of saturable absorber gratings.

We analyze and demonstrate a novel design for all-fiber tunable notch and bandpass loop-mirror filters (LMFs) with bandwidths ranging from the sub-MHz to beyond the GHz

regimes. Our narrowband LMF uses a straightforward configuration based on a loop mirror containing a saturable gain or absorber section. The LMF results from a grating that is formed by spatial hole burning in an active medium, induced by the interference pattern of a single pump beam that has been split and recombined. Our design uses a robust interferometrically-based method with built-in phase alignment of the signal to the pump-induced dynamic Bragg grating. In addition, since our loop can be short (less than 1 m), it does not suffer from problems typically associated with nonlinear optical loop mirrors such as large physical size, high latency, or extreme sensitivity to environmental fluctuations. Given the EDF used in our experiment, the filter is tunable in a few milliseconds (limited by the excited state lifetime of the erbium ions) by simply changing the wavelength of the pump light that establishes the intraloop grating. The filter may be operated with the pump and signal entering either the same or opposite ports of the 50/50 coupler located at the loop mirror input. Switching between gain and absorption changes the filter function changes between notch and bandpass, depending on the input ports chosen for the pump and signal.

The robust LMF configuration, shown in Figure 16, is simply a 50/50 coupler with the two outputs joined by a section of saturable gain or absorber. A standing wave created by counterpropagating pump waves creates a grating in the intraloop saturable medium. In the saturable gain case, the standing wave creates alternating regions with gain and without gain (where the gain is bleached). Similarly, alternating regions with and without absorption are created in the saturable absorber case. These gratings have a period of one-half the pump wavelength. When a secondary data signal is input to the loop mirror, it too creates a set of counterpropagating waves within the saturable medium. This data signal should have lower amplitude to avoid disturbing the original pump-induced grating. The gain or absorption experienced by this signal standing wave depends on its phase and periodicity relative to the grating induced by the pump standing wave. By choosing which of the two loop input ports is used for the pump and signal

waves, we can reconfigurably determine whether the interference patterns created by the two pairs of counterpropagating standing waves are exactly in phase (for the same input port) or π out of phase (for different input ports). This is due to the fact that light coupled across a coupler undergoes a $\pi/2$ phase shift relative to light coupled straight through. An important feature is that the relative phases of the pump and signal at the loop inputs are irrelevant.

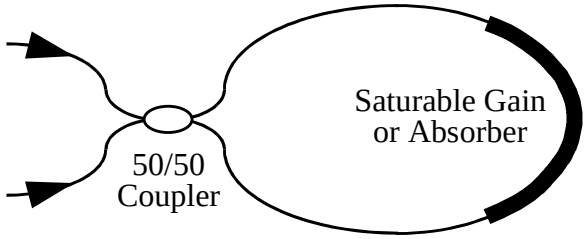

Figure 16. The loop-mirror filter is simply a fiber loop mirror containing a saturable gain or absorber section.

The LMF operates as follows. When the pump and the signal enter the loop through the same input and have the same frequency, the signal interference pattern will be in phase with the pump interference pattern. Hence, for a saturable gain, these signals experience the regions bleached by the pump and pass without gain. As the signal frequency begins to deviate from the pump frequency, the interference pattern phase matching condition will no longer be satisfied and these signals will be amplified, thereby creating a notch filter. The strongest amplification occurs when the interference patterns are π radians out of phase, where the signal standing wave coincides maximally with the regions where the pump has not bleached the gain. With further frequency deviation, the interference patterns become increasingly decorrelated, and amplification levels off to an intermediate value. If, however, the pump and the signal enter the loop through different ports, their interference patterns will be π radians out of phase. In this case, signals near the frequency of the pump will be amplified. As the signal frequency deviates from the pump frequency, the interference patterns will no longer be π radians out of phase and amplification will decrease, resulting in a bandpass filter.

For a saturable absorber, we have the opposite situation. When the pump and the signal enter the loop through the same port we have a bandpass filter, whereas if the pump and signal enter through different ports, we have a notch filter. Thus, simply by choosing the proper inputs for our signals we can create saturable gain or saturable absorber bandpass or notch filters. Using different input ports for the pump and signal permits convenient separation at the output of the signal and the pump, which are at similar frequencies.

The coupled differential equations for the normalized counterpropagating pump wave amplitudes, $A_{1\pm}(x)$, and signal wave amplitudes, $A_{2\pm}(x)$, in the saturable gain or absorber section are known [25]. When we write these equations in terms of pump and signal intensities, with $P_{\pm} = |A_{1\pm}|^2$, $S_{\pm} = |A_{2\pm}|^2$, they become:

$$\frac{dP_{\pm}}{dz} = \pm \frac{g_0}{\left(a^2 - b^2\right)^{\frac{1}{2}}} \left[P_{\pm} - \frac{a - \left(a^2 - b^2\right)^{\frac{1}{2}}}{2} \right]$$

$$\frac{dS_{\pm}}{dz} = \pm \frac{g_0}{\left(a^2 - b^2\right)^{\frac{1}{2}}} \left[S_{\pm} - \left(1 + \Omega^2\right)^{\frac{1}{2}} \left|A_{2+} A_{2-}\right| \frac{a - \left(a^2 - b^2\right)^{\frac{1}{2}}}{b} \cos\left(\mp 2\Delta k z + \phi_{21} + \varphi\right) \right]$$

where g_0 is the unsaturated gain ($g_0>0$) or absorption ($g_0<0$) coefficient, $a = 1 + \Omega^2 + P_+ + P_-$, $b = 2|A_{1+}A_{1-}|$, Ω is the detuning of the pump wave from the absorption resonance, Δk is the signal wavenumber offset from the pump (i.e., a measure of the phase mismatch between the pump and the signal waves), z is the distance measured from the center of the saturable medium, ϕ_{21} is the relative phase between the interference patterns of the counterpropagating pump and signal waves at $z = 0$, and $\varphi = arg[g_0(1 + i\Omega)]$.

Figure 17(a) shows narrow bandwidth notch filter responses (as a function of signal frequency offset from the pump wave) based on saturable gain gratings (EDF lengths 1.0, 0.7, and 0.5 m, $P_{\pm}$ = 7.0 dB, and g_0 = 14.5 m^{-1}). Figure 17(b) shows wider bandwidth bandpass filter

responses based on saturable absorber gratings (EDF lengths 0.2, 0.1, and 0.05 m, $P_{\pm}$ = -7.0 dB, and g_0 = -17.3, -34.5, and -69.1 m^{-1}). In each case the pump and signal are input to the same port of the 50/50 coupler, and $\Omega = \varphi = \phi_{21} = 0$. Similar results are obtained when the pump and signal are input to different ports of the 50/50 coupler.

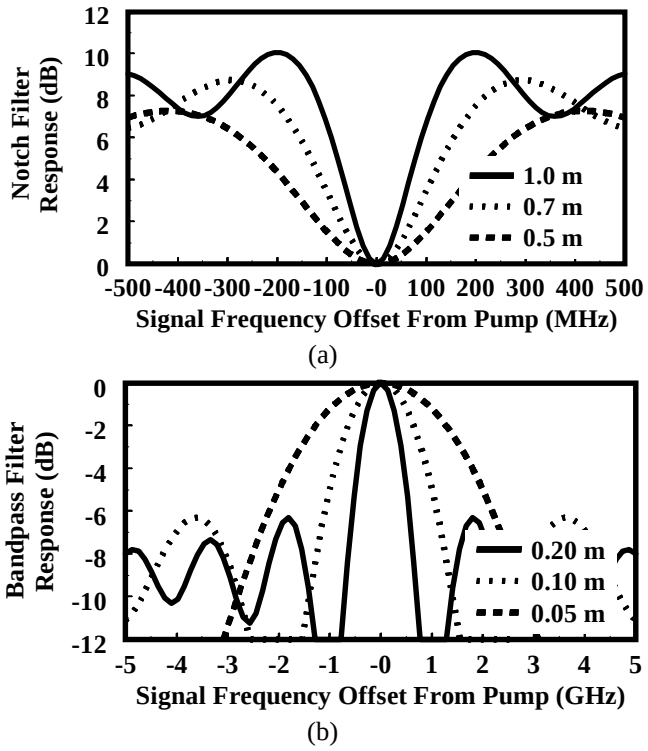

Figure 17. Theoretical response of (a) notch LMFs with saturable gain gratings, and (b) bandpass LMFs with saturable absorber gratings, for different EDF lengths.

The experimental setup used to measure LMF responses when the pump and signal enter the same port of the 50/50 coupler is shown in Figure 18. The parameters of the saturable medium are chosen based on the desired filter characteristics (e.g., bandwidth is approximately proportional to the inverse of the length of the saturable medium). A network analyzer makes calibrated measurements and provides the RF drive signal to the modulator. Modulating the optical carrier shifts a fraction of the power into sidebands. As the modulator RF input frequency

input is swept, these sidebands probe the filter response. The magnitude of the sidebands (signals) was adjusted to 30 to 40 dB below the carrier (pump) power. Note that the pump coherence length must be longer than the length of the saturable gain or absorber section, a requirement easily satisfied by commonly available lasers. The filter response is insensitive to the input state-of-polarization, but a polarization controller is used at each end of the EDF to maximize interference between the counterpropagating waves and ensure that the signal is coupled out through the proper port of the loop mirror. This setup did not allow the signal polarization to be adjusted independently of the pump polarization, but the two need not match. 980-nm light is coupled into the EDF for the saturable gain case. A similar configuration is used for LMF characterization when the pump and signal enter different ports of the coupler.

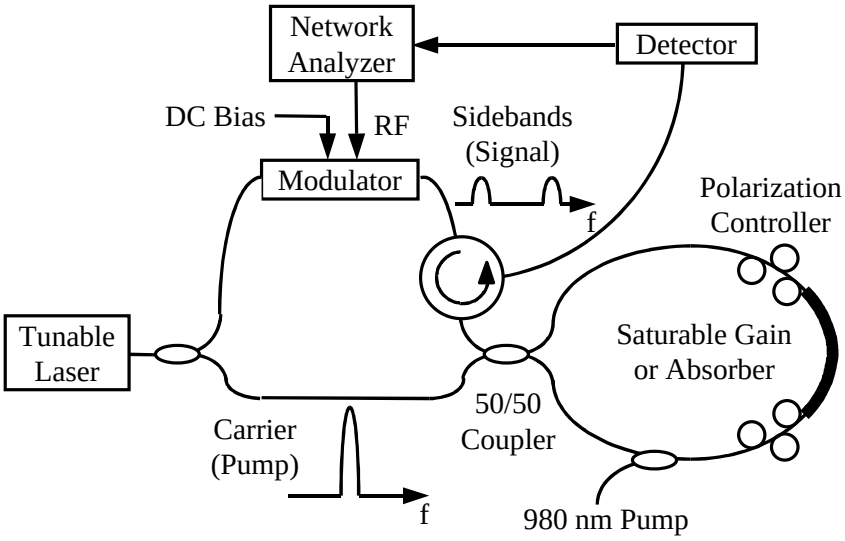

Figure 18. Experimental LMF characterization setup for the case where the pump and signal are input to same port of the 50/50 coupler.

Figure 19(a) shows the response measured with the configuration shown in Figure 18 for notch LMFs based on saturable gain gratings at 1525, 1530, and 1535 nm. These filters were created by use of a 1-m EDF with a peak absorption coefficient near 1530 nm of 14.5 m^{-1}. The power in each counterpropagating pump wave was 0 dBm. 20 dBm at 980 nm was coupled into

the loop to provide gain. Without the 980-nm input, gain becomes absorption, and the notch filters are converted to bandpass filters, as shown in Figure 19(b).

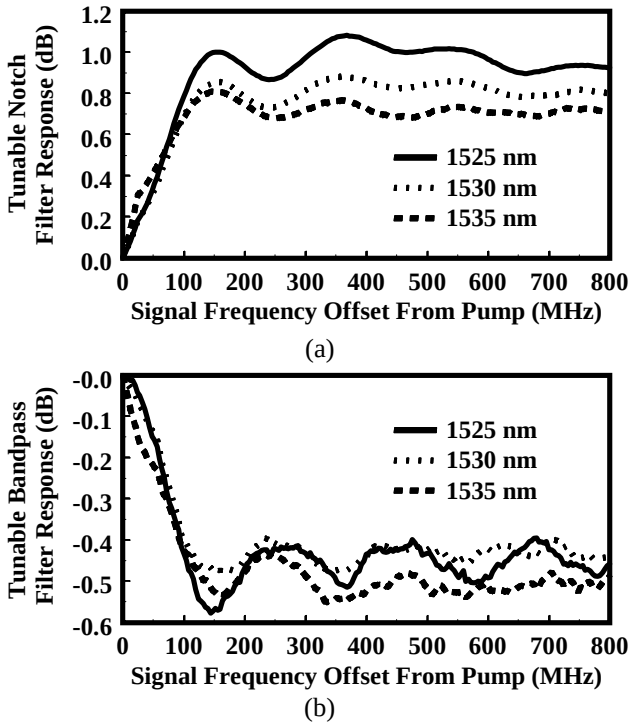

Figure 19. Measured response of (a) tunable notch LMFs with saturable gain gratings, and (b) tunable bandpass LMFs with saturable absorber gratings.

Experimental results match predicted filter shapes and bandwidths, but the measured filter strength is less than expected. Based on theoretical predictions, we believe that the experimental results could be improved significantly.

4. Applications of Subcarriers

4.1 Bit Synchronization Using Subcarriers for Control Signaling

As data rates increase in single-channel or wavelength-division multiplexed (WDM) optical networks, many aspects of optical switching performance must keep pace to maintain high throughput. For example, two different incoming bit streams must be synchronized before entering a 2x2 switching node in order to enable fast multiplexing, contention resolution, and switching [34, 49, 56]. Such synchronization should be on a bit-by-bit as well as on a packet-by-packet basis in order for the multiplexer or switch to operate with peak efficiency in the time domain [55, 57]. Bit synchronization is of particular importance in time-division multiplexed (TDM) systems, where data bit streams from different sources must be aligned before multiplexing to avoid bit overlap. In addition, all-optical approaches have the potential advantage of being able to handle higher-speed bit streams than electronic methods.

Previous work on all-optical synchronization has included techniques for both the delays and for the signaling. Methods for implementing the optical delay include the use of a series of optical crossbar space switches that are set to select a path for a bit stream through a matrix of delay lines [6, 28, 41], and wavelength tuning an optical transmitter over several nanometers to adjust the delay of the bits based on propagation through dispersive fiber [4]. Control signaling to determine the required delay has included framing pulse recognition [41], and header bits decoded through fully digital clock recovery [28]. These signaling methods have all required relatively complex digital logic. Alternatively, subcarrier tone recovery is completely in the RF domain and does not require electronic digital processing that may slow performance. Although subcarriers have been used to provide clock information at a receiver for recovering a data packet [6], subcarriers have not previously been employed as a signaling technique for bit synchronization between two incoming streams at a switching node. Moreover, in no case has synchronization using both optical signaling and delay been previously reported to within a fraction of a bit time.

We demonstrate bit synchronization of two incoming 1-Gb/s nonreturn-to-zero (NRZ) input signals using a subcarrier pilot tone superimposed on the data of each channel at a frequency equal to the channel data rate. At the synchronization module, each subcarrier is extracted and electronically mixed in real time with a local reference clock to generate an output electronic signal proportional to its relative phase differential. This phase-difference signal dynamically sets a matrix of crossbar space switches within a few nanoseconds to select the appropriate path-dependent delay for each incoming bit stream. Using three optical space switches in a feedforward structure, two 1-Gb/s signals are actively synchronized to within 125 ps (i.e., 1/8 of a bit time). This technique acquires the phase delay directly in the RF domain, does not require a high-speed clock recovery circuit, and can synchronize the two incoming bit streams to within a fraction of a bit time. The resolution of this method depends on the number of optical space switches and fiber delay lengths and can be easily scaled up to accommodate much higher bit rates.

The experimental setup is shown in Figure 20. Two NRZ data streams at 1 Gb/s (channel A at 1542 nm and channel B at 1552 nm) arrive at the synchronization module before entering a multiplexer or switching node. In order to demonstrate dynamic on-the-fly bit synchronization for this experiment, the data streams in both channels consist of data packets of length 432 bits separated by guard times of 18 ns. For each channel, the bit stream and the superimposed subcarrier are aligned at the transmitter such that the leading edge of each bit coincides with the zero-degree phase of the subcarrier. The 1-GHz subcarrier is derived directly from the same clock source as the data transmitter itself, thereby ensuring easy correlation between the data bit and the subcarrier. The subcarrier modulation depth (amplitude of subcarrier/(amplitude of subcarrier + amplitude of data)) is 10%.

The two main components in the synchronization module of Figure 20 are the RF synchronization electronics and the fiber delay stages. The fiber delay stage is a cascade of three space switches connected by fiber delay lines of different lengths corresponding to 1/8, 1/4, and

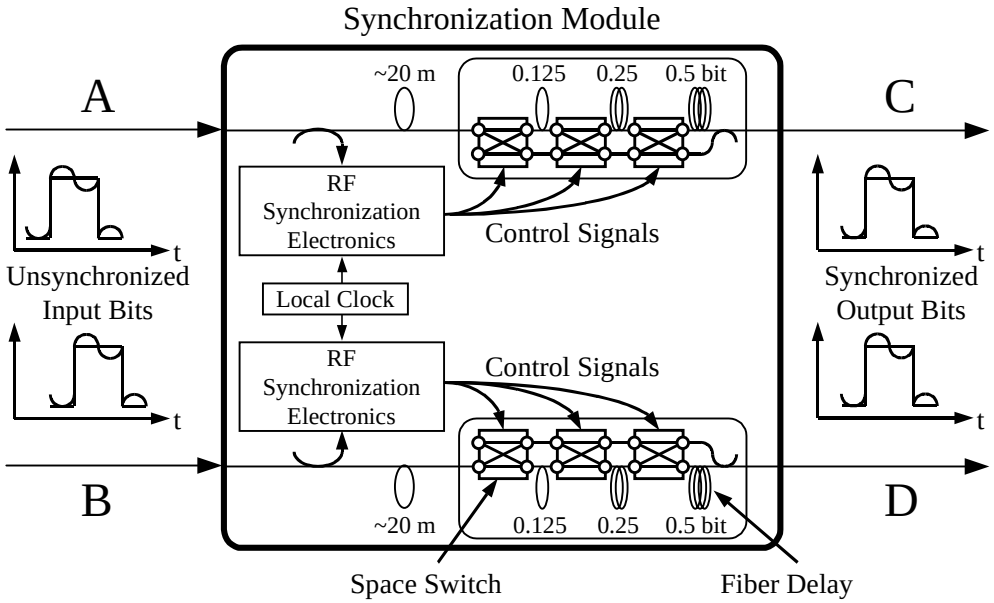

Figure 20. Experimental bit synchronization setup showing unsynchronized input bits and synchronized output bits. The RF synchronization electronics use a fraction of the incoming optical signal to determine the bit offset and send control signals to the fiber delay stages. The synchronization module uses a matrix of crossbar space switches and delay lines in a feedforward configuration to synchronize the signals to a local clock.

1/2 of a bit time. The synchronization electronics includes frequency mixers, filters, and an ECL circuit board that controls the operation of the fiber delay stages. At the input to the synchronization module, 10% of each incoming channel is tapped off by an optical coupler, then detected and input to the RF synchronization electronics. A portion of this tapped signal is sent to the packet flag detection unit to determine the arrival of a data packet. We use 8 consecutive "1" bits as the packet flag. Other lengths can also be used as long as there is no potential for confusion with any data bit pattern in the packet payload. The rest of the tapped signal is passed through an RF bandpass filter centered on the subcarrier frequency at 1 GHz in order to extract the subcarrier from the data. The extracted subcarrier is passed through a 3-dB power splitter and the outputs are frequency mixed with two quadrature signals (sine and cosine) derived from the 1-GHz local clock to produce two phase differential signals which uniquely identify (from 0 to 360°) the correct signal phase delay. Details of the frequency mixing technique are shown in Figure 21. A 3-bit A/D

converter digitizes the phase differential signals and compares the results to a built-in lookup table to convert the phase differential signals to a time offset relative to the local clock. This time offset is used to generate control signals that are applied to the space switches in order to select the appropriate routing of each channel through the space switches and fiber delay lines. By aligning each channel to the local clock, the channels are effectively synchronized to each other. The control signal for each space switch is generated simultaneously by the RF synchronization electronics. However, the signals must be delayed electronically so each switch gets set during the guard time before the packet arrives at the switch. In addition, a short fiber delay (~20 m) is used after the tap to the RF synchronization electronics to match the propagation time of the signal through the electronics.

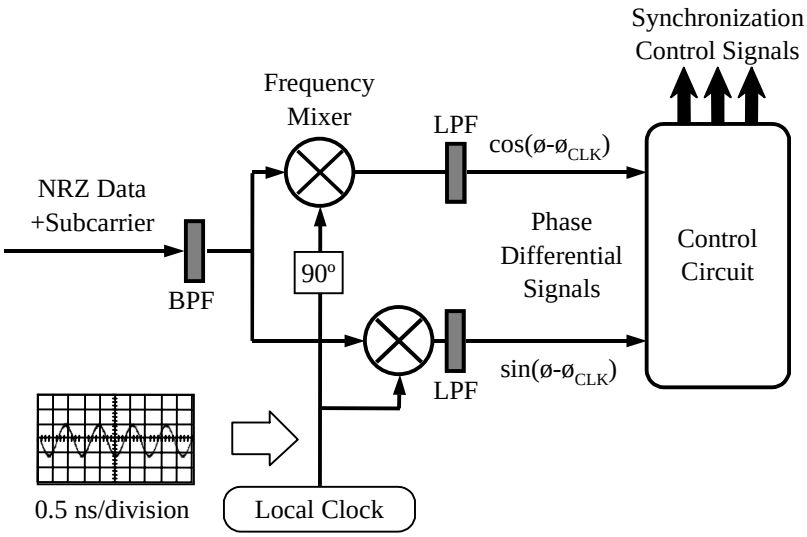

Figure 21. Details of the frequency mixing technique. The extracted subcarrier passes through a power splitter and the outputs are mixed with the quadrature signals from the local clock. The frequency mixing products are used by the control electronics circuit board, which sends control signals to the three crossbar space switches.

Figure 22 shows the RF spectra and the oscilloscope traces of the baseband and RF subcarrier for channel A. Figure 22(a) shows the baseband data with the subcarrier superimposed at the output from the transmitter. The 1-GHz subcarrier falls exactly between the main lobe and

first side lobe of the 1-Gb/s NRZ data spectrum, i.e. at the null of the spectrum, and, therefore has minimal influence on the baseband data. The subcarrier modulation depth at the transmitter is ~10% which leads to a power penalty of less than 1 dB [33]. Figure 22(b) shows an RF spectrum and oscilloscope trace of the recovered subcarrier.

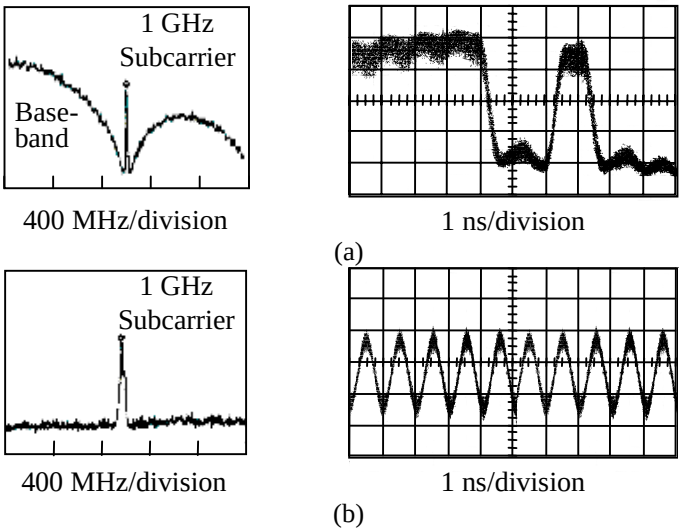

Figure 22. The RF spectra and oscilloscope traces for the 1-Gb/s NRZ baseband and 1-GHz RF subcarrier clock of an incoming channel (a) before and (b) after RF filtering.

Experimental results for bits from channel A and channel B packet streams input to the synchronization module are shown in Figure 23. Incoming unsynchronized bits and dynamically synchronized output bits for channel A and channel B are shown against the local clock. The input bit streams on channel A and channel B are intentionally offset by 500 ps and 125 ps, respectively, relative to the local clock. After the synchronization module, the bits in both channels are synchronized to each other. The minimum time needed for synchronization is determined by the speed of the RF recovery (<1 ns), control circuit board (<1 ns), and optical space switches (<1 ns).

Our synchronization technique assumes that the subcarrier and the local reference clock are matched in absolute frequency. However, an error will occur if the frequency walk-off between the two clocks is greater than 1/8 of a bit time over the length of the packet. A typical

OC-48 SONET multiplexer features a line rate of 2.48832 Gb/s ± 20 ppm [3], and local oscillators are available with much higher accuracy. Therefore, by simply selecting commercially-available components, our synchronization module can accommodate packet lengths up to 6250 bits without error.

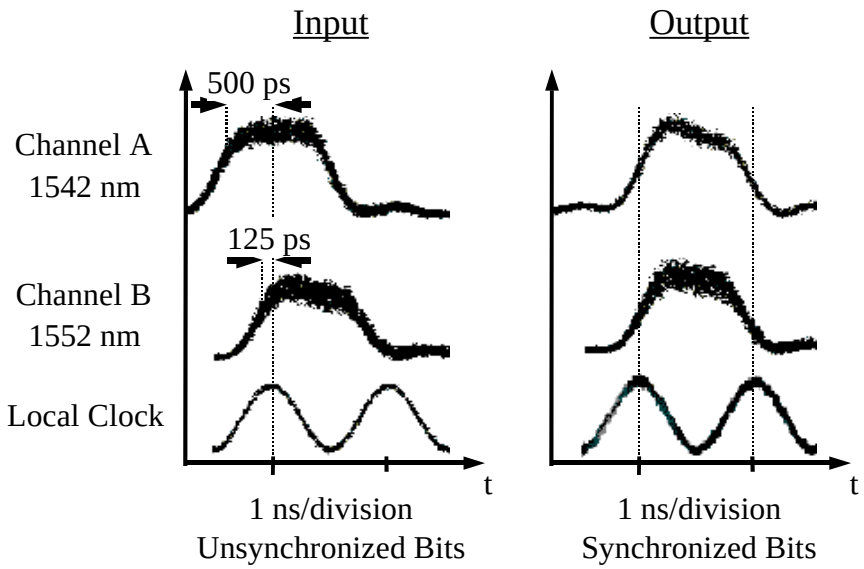

Figure 23. Unsynchronized input and synchronized output bits from the module for channel A at 1542 nm, channel B at 1552 nm, and the local reference clock. The time offsets of the input bits from the two channels are intentionally set to 500 and 125 ps with respect to the reference clock.

4.2 Optical Output-Port Contention Resolution using Subcarrier Multiplexing

For future high-throughput dynamically-reconfigurable optical networks, it is desirable to ensure efficiency in the switching process at each node. Consequently, output-port contention, in which two data packets located at the same wavelength and at two different input ports request to be routed to the same output port, must be rapidly resolved. All-optical contention resolution has the potential to enable high-speed on-the-fly processing. In conventional network architectures, contention may be resolved by two techniques, both of which induce signal latency and decrease network throughput: (i) local buffering of the contending packets until the desired output port is available, which is difficult to accomplish in the optical domain, or (ii) deflection routing of the

contending packets out a suboptimal port, after which the packets will eventually arrive at their ultimate destination. A laudable goal for highly-efficient networks is to route all data packets out their desired port without incurring additional latency [36]. The most common technique for sending all packets out their desired ports is to wavelength shift one of the contending packets onto a free wavelength at the preferred output port in a wavelength-division multiplexed (WDM) network [7]. Unfortunately, given the limited number of wavelengths available in fiber systems, there may not be unused wavelengths reserved for achieving contention resolution. By using subcarrier-multiplexing techniques, we pursue an alternate all-optical approach that is spectrally efficient and maintains low switch latency.

Here we demonstrate an all-optical contention resolution switching technique for two identical-wavelength contending incoming 2.5 Gb/s channels by upconverting one packet to a higher microwave frequency, f_{CR}, beyond the other channel's baseband signal, as shown in Figure 24. Although one channel is shifted to a higher frequency, the shift is small enough such that both channels appear to be the same wavelength channel when traversing any wavelength-selective elements in a WDM network. We employ narrow (~5 GHz) fiber Fabry-Perot (FPF) filters to optically demultiplex the two contending channels at the receiver, with a power penalty <1 dB. Even though the microwave subcarrier frequency of the resolved packet is higher than the channel's original baseband signal, the receiver electronics need only be as fast as the baseband data rate itself. Furthermore, this spectrally efficient subcarrier-multiplexing method enables contending packets to maintain their original wavelengths for optimal routing through the network.

Figure 25 shows the experimental setup of the contention resolution node for two identical-wavelength channels. We employ an optical Mach-Zehnder $LiNbO_3$ modulator to achieve all-optical frequency upconversion [20, 40]. In the contention resolution node, optical power is tapped in order to detect output wavelength contention by monitoring the data packets on

each input port. In case of contention, an optical modulator at minimum bias optically upconverts one of the contending channels, i.e., channel 2, to a microwave subcarrier frequency (f_{CR}), thereby shifting copies of the baseband information up and down by the subcarrier frequency. Minimum-biasing the modulator suppresses by >30 dB both the optical carrier and the unwanted original baseband signal of the upconverted channel 2. The original channel 1 and the upconverted and downconverted channel 2 are then combined before exiting the node.

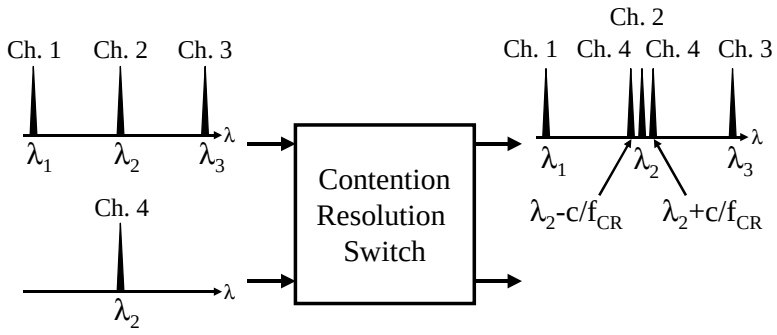

Figure 24. Conceptual diagram of our contention resolution technique. Channel 4 is optically upconverted to a higher microwave frequency f_{CR} and then combined and routed out the same output port as the other channels.

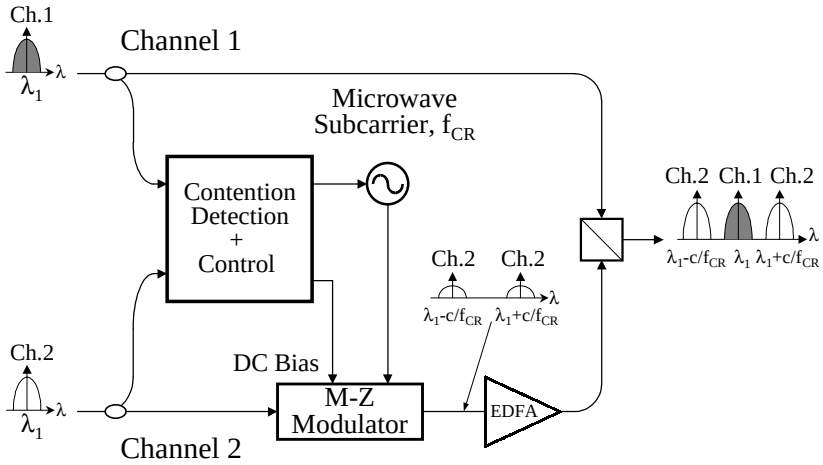

Figure 25. The setup of the contention resolution node. A minimum-biased Mach-Zehnder modulator optically upconverts channel 2 beyond the baseband signal of channel 1.

Due to the beating effects of the optical sidebands in the photodetector itself, the two channels cannot be independently recovered with a single high-speed receiver. Using a single receiver would lead to mixing products at baseband, the subcarrier frequency f_{CR} and all higher harmonics, thus making impossible the recovery of the individual channels. Therefore, we use optical demultiplexing with narrowband tunable fiber Fabry-Perot (FPF) filters [16]. By optically filtering either the baseband of channel 1 or one of the two sidebands of channel 2, the photodiode detects the original baseband signal of either optical channel. Optical filtering negates the need for electronic downconversion, and enables the receiver to operate at the lower data baseband frequency rather than at the higher subcarrier frequency. The receiver setup is shown in Figure 26.

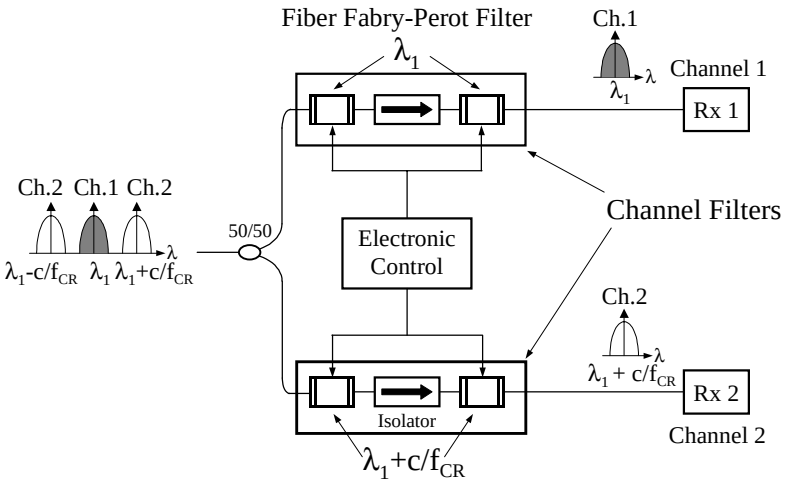

Figure 26. The setup of the demultiplexing receiver. Cascaded fiber Fabry-Perot filters perform channel selection before detection using baseband receivers.

Two cascaded FPFs are tuned electronically to the frequency of the desired baseband signal of channel 1 and one sideband of channel 2. The filter package is temperature stabilized using a feedback control to obtain a constant center frequency of the FPF. The isolator between the FPFs is necessary to avoid multiple reflections within the interfilter cavity [46]. Figure 27 depicts the measured transfer characteristics of the FPFs with a 3-dB bandwidth (FWHM) of 8 and 5 GHz for

the individual and cascaded FPFs, respectively. Cascading two FPFs improves the rejection of the unwanted neighboring signals by more than 15 dB compared to using a single FPF.

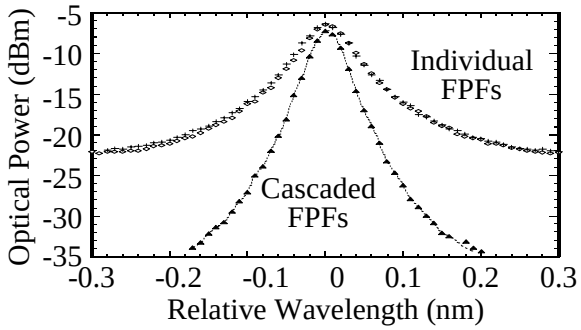

Figure 27. Measured characteristics of the single and cascaded fiber Fabry-Perot filters (FPFs). The bandwidth of the cascaded FPFs is ~5 GHz.

In order to test the different elements of our technique, we first optically upconvert channel 2 without combining it with the baseband channel 1. The cascaded FPF configuration is employed to demultiplex one optical sideband of channel 2 at the receiver. Figure 28(a) shows the measured optical power penalty at a bit error rate (BER) of 10^{-9} for subcarrier frequencies ranging from 6 to 12 GHz at a microwave power level of +16 dBm and a data rate of 2.5 Gb/s. A slightly higher power penalty for f_{CR} = 6 GHz is observed due to the crosstalk of the residual baseband signal of channel 2 caused by the finite extinction ratio of the minimum-biased modulator.

The microwave power level of the subcarrier determines the amount of optical power shifted into the sidebands of the upconverted data signal. A fixed subcarrier frequency of f_{CR} = 8 GHz is used to examine the effects of different subcarrier power levels. The baseband channel 1 is not added to avoid any crosstalk penalty, therefore isolating the effects of the different microwave power levels on the upconversion process. Figure 28(b) shows the optical power penalty at BER = 10^{-9} for the upconverted channel 2 versus the applied microwave power of the subcarrier. A power penalty <1 dB can be achieved by using microwave power levels of more than +13 dBm for the subcarrier.

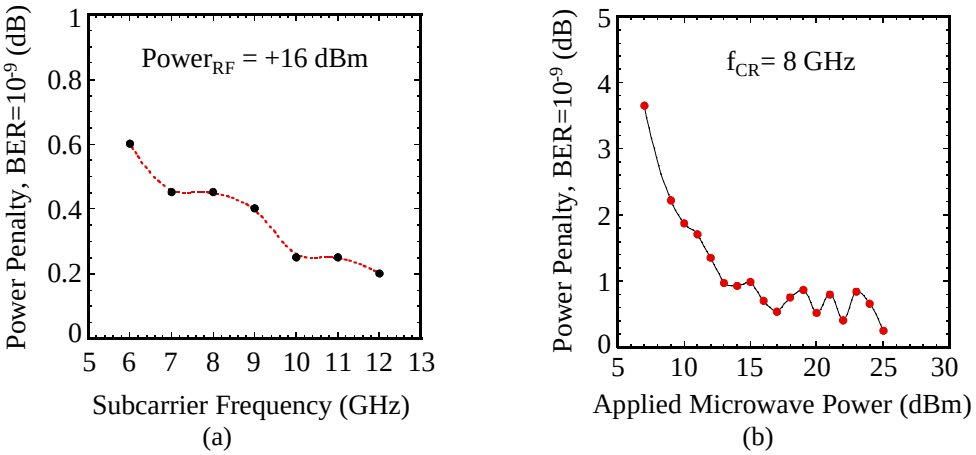

Figure 28. Measured optical power penalty at BER = 10^{-9} for channel 2 without combination with channel 1 (a) versus subcarrier frequency, f_{CR}, with an applied microwave power of +16 dBm, and (b) versus applied microwave power at a subcarrier frequency of f_{CR} = 8 GHz.

To demonstrate full contention resolution with our technique, we use two identical-wavelength 2.5 Gb/s channels, each incident to a single input port. Figure 29(a) shows BER measurements for both channels in the complete system for +16 dBm subcarriers at 6 and 12 GHz. The ~2 dB power penalty at f_{CR} = 6 GHz can be attributed to crosstalk between the closely spaced

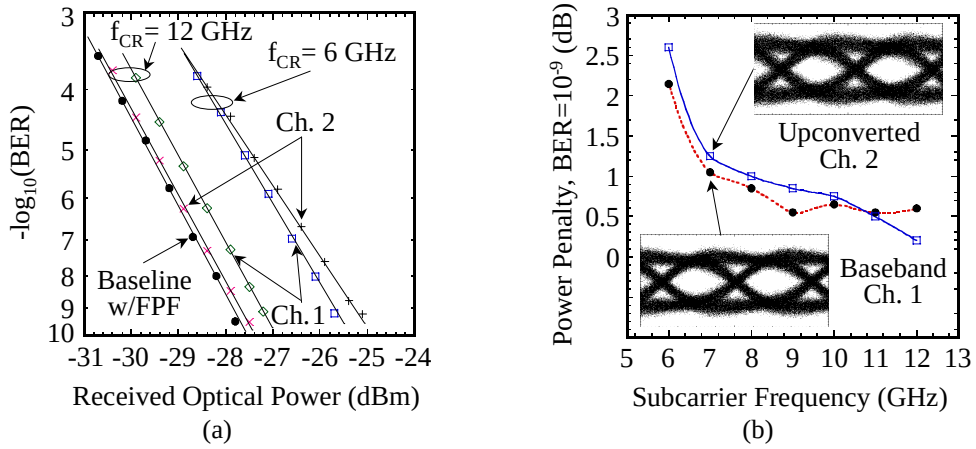

Figure 29. (a) BER measurements for both channels at subcarrier frequencies f_{CR} = 6 and 12 GHz and an applied microwave power of +16 dBm. (b) Measured optical power penalty at BER = 10^{-9} for both channels at subcarrier frequencies from f_{CR} = 6 to 12 GHz and an applied microwave power of +16 dBm. Insets show received eye diagrams for the baseband and upconverted channels (data rate = 2.5 Gb/s).

optical sidebands of both channels. At f_{CR} = 12 GHz, the power penalty decreases to ~0.6 dB for channel 1 and <0.2 dB for channel 2 due to lower crosstalk. The higher power penalty for channel 1 is caused by the residual baseband signal of the upconverted channel 2. This crosstalk-induced power penalty at BER = 10^{-9} is seen in Figure 29(b) for subcarrier frequencies ranging from 6 to 12 GHz. The power penalty of channel 1 levels out at ~0.6 dB for frequencies $f_{CR} \geq 9$ GHz. The power penalty for channel 2 decreases steadily to <0.2 dB at f_{CR} = 12 GHz, due to greater separation and lower crosstalk between the two channels.

Our technique can resolve two contention resolution events on the same wavelength using an identical subcarrier frequency (8 GHz), by placing cascaded FPFs directly after the modulator in the upconversion node to select only one of the resulting upconverted sidebands (data rate = 2.5 Gb/s). Higher subcarrier frequencies (16 GHz) beyond the first upconverted channel could also be used to resolve additional contention events, further reducing the packet blocking probability in an optical network [29]. Moreover, higher data rates, such as 10 Gb/s, can be accommodated with our technique by increasing the subcarrier frequency to about 30 GHz and employing cascaded FPFs with a bandwidth of ~20 GHz. This scheme is only limited by the overall wavelength spacing of the channels, with a minimum allowable spacing of 50 GHz for a data rate of 2.5 Gb/s and 200 GHz for a data rate of 10 Gb/s.

4.3 Distance-Independent Microwave and Millimeter-Wave Power Fading Compensation Using a Phase Diversity Configuration

An increasing number of applications require transmission of analog or digital subcarrier-multiplexed (SCM) microwave or millimeter-wave channels over optical fiber. However, transmitting traditional double-sideband (DSB) signals is problematic due to chromatic dispersion. This frequency-dependent fiber dispersion produces a deleterious time delay of the two transmitted sidebands relative to the optical carrier, causing serious dispersion-induced power fading that is a function of subcarrier frequency, fiber distance, and accumulated dispersion [48].

Unfortunately, many potential applications involve reconfigurable optical paths, where power fading dynamically changes with transmission distance. For robust microwave- and millimeter-wave-based optical systems, distance-independent power fading compensation is highly desirable.

Several approaches have been proposed to compensate for dispersion-induced power fading in conventional DSB systems, including adjustable modulator chirp [19] and linearly-chirped fiber Bragg gratings (FBGs) [35]. But these techniques are dependent on transmission distance and must be actively tuned to accommodate different transmission path lengths. We have previously reported the use of a nonlinearly-chirped fiber Bragg grating to provide tunable compensation for dispersion-induced power degradation in variable-length multiple-channel SCM transmission links [53]. This grating has the ability to uniquely provide a tunable dispersion to incoming signals since the time delay as a function of wavelength has a nonlinear shape. However, this technique also suffers from being transmission length dependent. Minimum transmission modulator biasing [18] and single-sideband (SSB) transmission [50], which are relatively immune to the problem of dispersion-induced power fading, have also been proposed. But minimum transmission modulator biasing requires additional control circuitry to maintain the modulator bias point and may introduce additional distortions in the signal, while SSB transmission requires additional electrical components to implement, and multiple SSB-generating circuits may be required to cover the entire frequency range of multiple-channel SCM systems. It has also been recently shown that chirped FBGs are significantly more effective than SSB transmission at compensating for dispersion-induced nonlinear distortion in multiple-channel SCM systems [42].

We use a tunable nonlinearly-chirped FBG in a phase diversity configuration to achieve distance-independent power fading compensation for DSB SCM systems. In our technique, the incoming signal is split into two components, and an extra π phase shift relative to the optical carrier is induced in the modulation sidebands of one optical path relative to the other by reflection off the stretched nonlinearly-chirped FBG. At the output of this phase-diversity configuration,

orthogonally-polarized components of the signals in the two paths are combined to reduce coherent crosstalk effects. We demonstrate distance-independent compensation of dispersion-induced power fading from 0 to 150 km for 8- and 12-GHz subcarrier frequencies, with received subcarrier power in all cases uniform to within 1 dB. Error-free transmission is also achieved for 0-, 27-, and 52-km transmission of a 155-Mb/s SCM/amplitude-shift-keyed channel.

The concept behind our distance-independent power fading compensation technique is illustrated in Figure 30(a). Without compensation, the received subcarrier power, $P_{el,f}$, is a function of transmission distance, with periodic power drop-outs [48]:

$$P_{el,f} \propto \cos^2\left(\frac{\varphi_1 + \varphi_2}{2}\right) = \cos^2\left[\pi c L D\left(\frac{f}{f_c}\right)^2\right]$$

where φ_1 and φ_2 are the phases of the modulation sidebands relative to the optical carrier, c is the speed of light, L is the transmission distance, D is the dispersion, f is the subcarrier modulation frequency, and f_c is the optical carrier frequency. In our compensation module, the tunable nonlinearly-chirped fiber Bragg grating in one path induces an additional relative phase shift of π in the modulation sidebands, as shown in Figure 30(b), resulting in a received electrical power that is again a function of distance, with periodic power dropouts. However, the different relative phases of the modulation sidebands in the two paths cause the power dropouts in the signal through one path to occur at different distances than the dropouts in the other path. Since the incident optical signals are orthogonally polarized, they do not interact in the photodetector. However, after photodetection, these two optical signals result in a pair of currents, one from the path containing the grating (I_g) and one from the other path (I_o):

$$I_g \propto c_g \cos\left(\frac{\varphi_1 + \varphi_2 + \pi}{2}\right)\cos\left(2\pi f t + \theta_g\right)$$

$$I_o \propto c_o \cos\left(\frac{\varphi_1 + \varphi_2}{2}\right)\cos\left(2\pi f t + \theta_o\right)$$

where c_g and c_o are constants representing the optical powers from the two paths incident on the photodetector, and θ_g and θ_o represent the relative subcarrier phases in the two paths. By properly combining these signals (i.e., setting the optical powers in the two paths equal and introducing an additional optical delay between the two paths of the module such that θ_g - θ_o = $\pi/2$), the total received subcarrier power is constant, and independent of the transmission distance:

$$P_{el,f} = \cos^2\left(\frac{\varphi_1 + \varphi_2}{2}\right) + \sin^2\left(\frac{\varphi_1 + \varphi_2}{2}\right) = \text{constant}$$

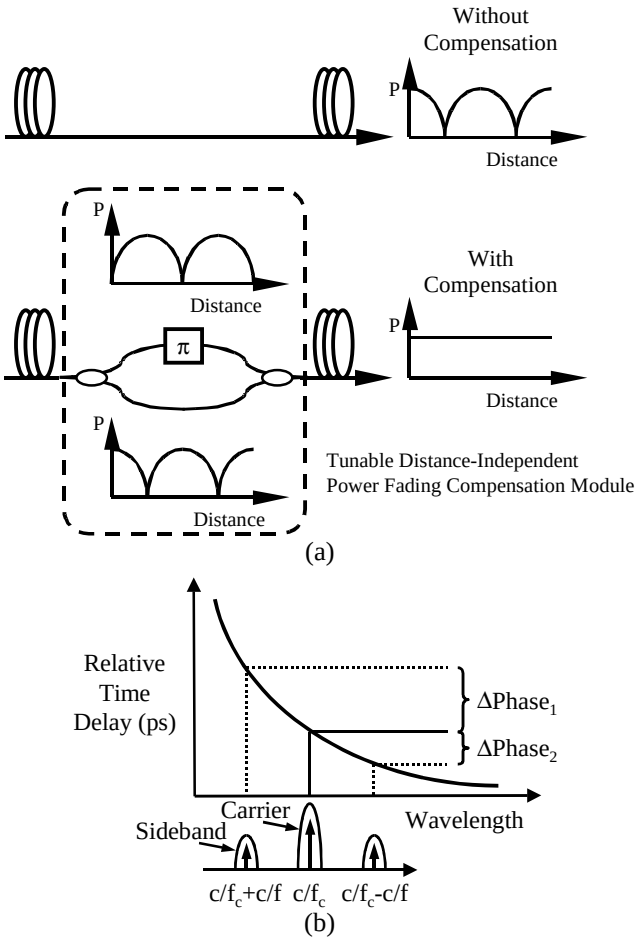

Figure 30. (a) Conceptual diagram of our phase diversity technique for distance-independent power fading compensation. (b) Effect of grating on the relative phases of the sidebands.

Details of the implementation of our module are shown in Figure 31. The splitting ratio at the input to the module is adjusted to compensate for different losses in the two paths. The grating is attached to a piezoelectric transducer (PZT), which stretches the grating to provide the required relative phase shift of the modulation sidebands in that path. The combination of a polarization controller with a polarization beam splitter permits recombination of the signals from the two paths with minimum coherent crosstalk. The optical path lengths of the two paths are matched at the required grating voltage, and then offset by a length corresponding to a subcarrier phase of $\pi/2$. With this adjustment, received subcarrier power is independent of distance.

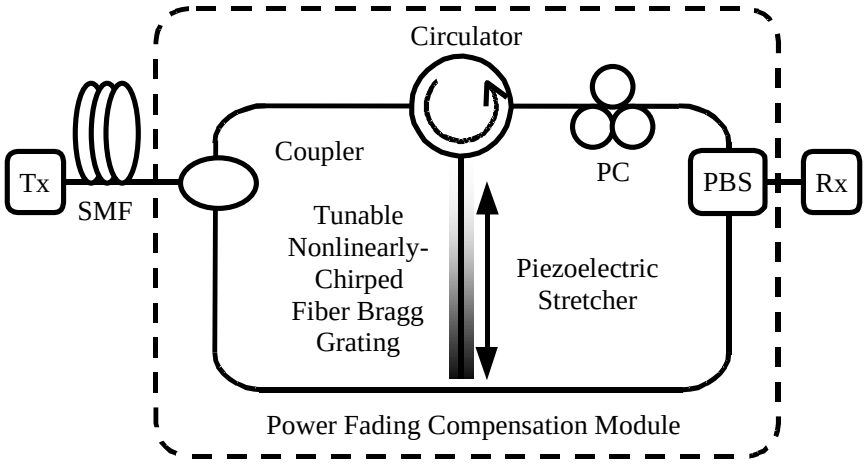

Figure 31. Distance-independent power fading compensation module. The lengths of the upper and lower paths are phase matched, then an extra $\pi/2$ phase shift is applied to one path to eliminate ripple in the received subcarrier power. Tx = transmitter, Rx = receiver, SMF = single-mode fiber, PBS = polarization beam splitter, PC = polarization controller.

Figure 32 shows the characteristics of our grating. Figure 32(a) depicts the shift in the nonlinear delay curve as we tune the grating control voltage. Note how the dispersion slope changes at a fixed wavelength as the grating control voltage varies. Figure 32(b) shows measured data indicating that distance-independent compensation from 7 to 13 GHz can be provided with our grating by tuning the grating control voltage from 0 to 500 V. The minimum frequency is limited by the maximum available dispersion slope, but since $\varphi_1 + \varphi_2$ is proportional to f^2, the

same grating could be used for compensation at much higher frequencies, as shown by the theoretical curves in Figure 32(b).

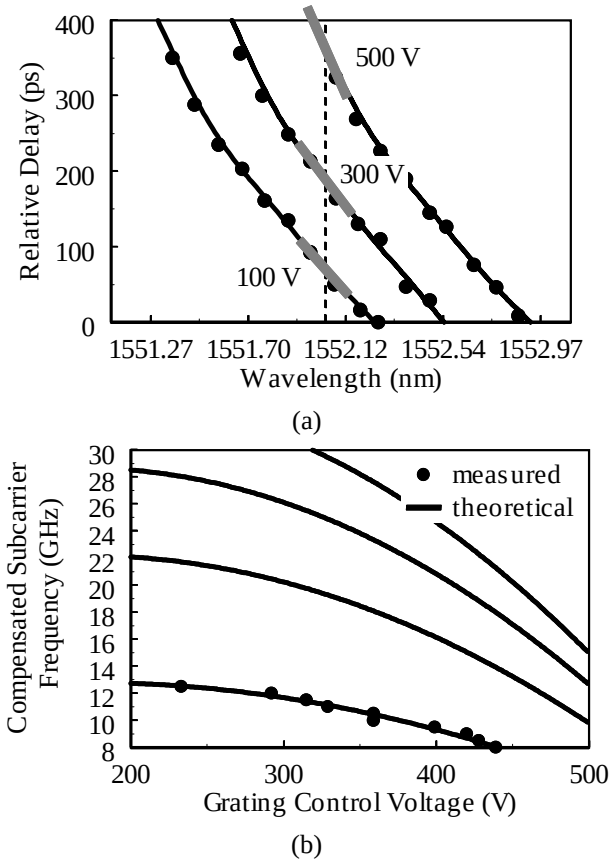

Figure 32. Grating characterization curves. (a) Wavelength shift of the nonlinear delay curve for different applied grating voltages. (b) Frequency at which power fading is compensated using our module as a function of applied grating voltage.

Performance (normalized to remove the 6-dB electrical power penalty) of our compensation module for 8- and 12-GHz subcarriers is shown in Figure 33 against theoretical and measured fading for uncompensated transmission distances up to 150 km. In both cases, the received subcarrier power after compensation using our module is uniform to within 1 dB.

To measure bit error rate (BER), 155 Mb/s pseudorandom data was electrically multiplexed to 8 GHz and transmitted as shown in Figure 34. BER measurement results are shown

in Figure 35. Error-free transmission is achieved at 0, 27.7, and 52.4 km. Note that at 8 GHz, 0 km corresponds to maximum power fading in the grating path of our module, while 52.4 km corresponds to maximum power fading in the nongrating path. Thus BER performance is independent of whether the received electrical subcarrier power originated from the grating path or the nongrating path. The 3-dB optical power penalty (6-dB electrical power penalty) relative to our back-to-back BER measurement comes from optical power splitting in our phase diversity technique.

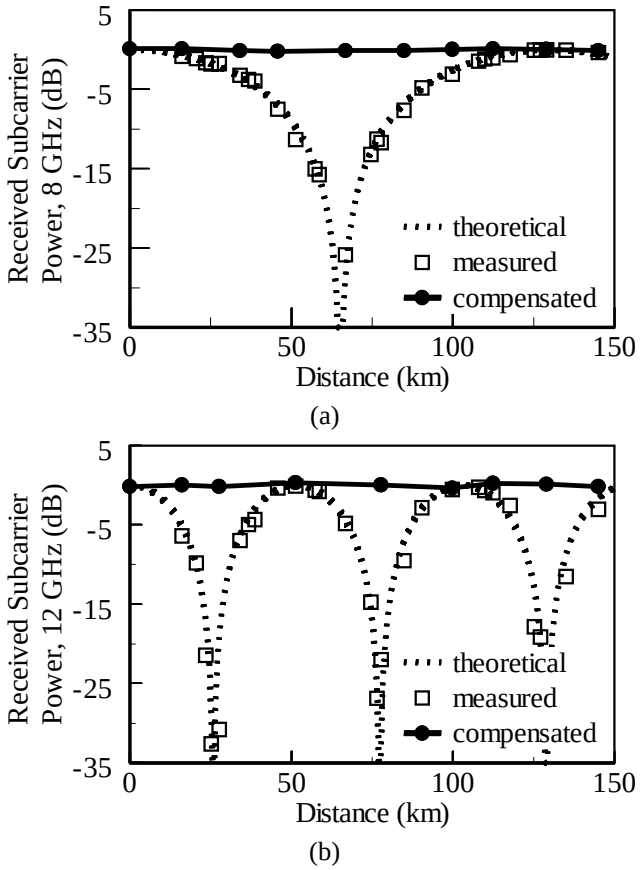

Figure 33. Compensated transmission over 150 km against measured and theoretical power fading at (a) 8 GHz and (b) 12 GHz.

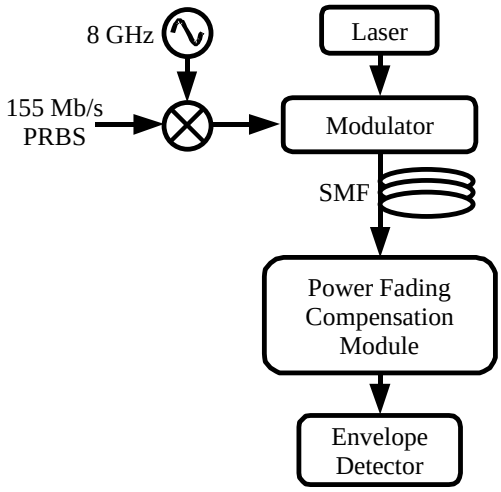

Figure 34. Electrical multiplexing with input electrical power spectrum and received bits.

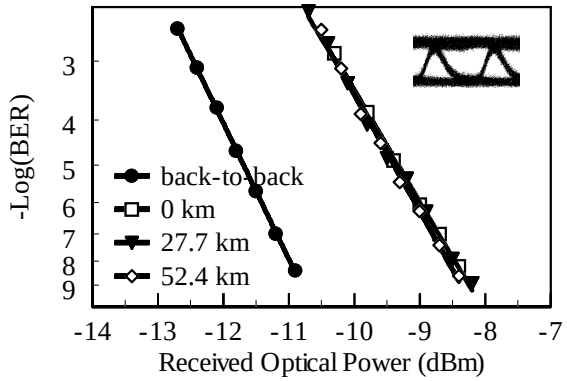

Figure 35. BER measurements.

Note that our module is effective at any location between the transmitter and receiver. In fact, locating the module at the transmitter may simplify polarization control and power balancing.

5. Conclusion

Despite the fact that current fiber-based optical communication systems use digital on-off modulation, I have shown that analog subcarriers can be used successfully in such systems to provide solutions to some of the problems that must be resolved in order to realize next-generation high-capacity, reconfigurable optical systems and networks.

My research has focused on several novel aspects of using subcarriers in optical communication systems, including (i) the generation of subcarriers, by either external modulation or optical heterodyning, (ii) narrowband tunable optical filters for routing or processing subcarriers, and (iii) applications which use subcarriers, such as synchronization, contention resolution, and tunable dispersion compensation.

The simplest technique to generate optical subcarriers is external modulation. To retain the advantages of low-biased external modulation while overcoming the inherently poor efficiency of this technique, I have developed an optically-efficient RF modulator that uses a novel arrangement of two low-biased Mach-Zehnder modulators within a ring laser. The dual Mach-Zehnder modulators eliminate resonances due to the relaxation oscillation and laser cavity modes allowing operation over a wide bandwidth. This configuration also preserves the modulator transfer function and provides single-frequency output. In addition, by recirculating the unused output of the first Mach-Zehnder modulator, optical efficiency is improved by over seven dB relative to a similar externally-modulated configuration. This technique may be useful in analog photonic links when available dc power is limited.

A very flexible technique for generation of subcarriers, especially at frequencies beyond the range of commercially-available external modulators and drivers (10 to 40 GHz), is optical heterodyning. In optical heterodyning, two lasers are mixed to generate a beat signal at a frequency corresponding to the wavelength difference between the laser outputs. These lasers each

must have a high spectral purity, and should be tunable. I have investigated both of these aspects. Using a delayed self-heterodyne interferometer and a narrow-linewidth fiber laser, I have studied the evolution of the interferometer output beat signal with increasing fiber delay. I demonstrated the importance of a long fiber delay and a Voigt fit to the interferometer output data to determine the true fundamental linewidth of a narrow-linewidth fiber laser. For my laser, I measured a Lorentzian linewidth of 750 Hz for fiber delays greater than 70 km. I also demonstrated a stable narrow-linewidth single-mode erbium-doped fiber ring laser with a 40-nm tuning range of 1522 to 1562 nm. The wide tunability is achieved using a highly-stretchable fiber Bragg grating that exhibits a filter tuning range of over 50 nm. This represents a 3.5-fold increase in wavelength tuning range over prior art using FBGs.

Filtering of subcarriers should be done in the optical domain to avoid electronic processing bottlenecks and costly optical-to-electrical-to-optical conversions. To solve this problem, I presented a novel all-fiber narrowband filter based on pump-induced saturable gain or absorber gratings in a loop mirror. This design provides built-in interferometric phase alignment of the signal to the grating for optimal filtering. Notch or bandpass functionality is determined by the choice of gain or absorption and the input ports selected for the pump and signal. The loop-mirror filter has potential bandwidths from the sub-MHz to beyond the GHz regimes, and is optically tunable by changing the wavelength of the pump light that establishes the grating. Such filters have potential applications to wavelength-division multiplexed optical networks and optical RF signal processing.

In terms of applications of subcarriers, synchronization is an important function that may be required in future optical networks. Fast and efficient routing, multiplexing, and contention resolution all require the incoming bit streams to be synchronized before entering a network switching node. I demonstrated bit synchronization of two 1-Gb/s NRZ input signals to within 125 ps (1/8 of a bit time) using a subcarrier as the control signal for determining the time delay

between the two baseband channels. The 1-GHz subcarrier for each channel is superimposed onto the baseband data at the transmitter, then recovered and mixed in real time with a local clock at the switching node to generate a signal proportional to the relative phase differential. This phase differential signal is used to dynamically set optical space switches thereby controlling the path through a matrix of delay lines. Each channel is independently synchronized to the local clock, resulting in the synchronization of the two output streams to within a fraction of a bit time.

Another application where subcarriers can be useful is contention resolution. Contention resolution without optical buffering or deflection routing can reduce network traffic delays. I demonstrated an optical contention resolution technique that combines two identical-wavelength contending 2.5 Gb/s channels into the same output-port wavelength channel. This is achieved by optically up-converting one channel to a higher microwave frequency beyond the other channel's baseband signal and routing both channels out the desired output-port wavelength channel simultaneously. By using narrow (~5 GHz) fiber Fabry-Perot filters for optically demultiplexing the two channels, I recovered each channel using a baseband receiver with <1 dB power penalty.

Finally, because dispersion can cause serious power fading in subcarrier-multiplexed transmission. I used a nonlinearly-chirped FBG in a phase diversity configuration to achieve distance-independent power fading compensation for DSB subcarrier-multiplexed systems. I demonstrated compensation for dispersion-induced power fading from 0 to 150 km at 8 and 12 GHz, with received subcarrier power in all cases uniform to within 1 dB.

6. References

[1] Ackerman, E., S. Wanuga, D. Kasemset, A. S. Daryoush, and N. R. Samant, “Maximum Dynamic Range Operation of a Microwave External Modulation Fiber-Optic Link,” IEEE Transactions on Microwave Theory and Techniques, **41**, 1299, 1993.

[2] Adamczyk, O. H., S. A. Havstad, A. B. Sahin, M. C. Cardakli, S. Lee, and A. E. Willner, “Optical Subcarrier-Multiplexing for Output-Port Contention Resolution,” accepted for publication, IEEE Photonics Technology Letters, **12**, TBD, 2000.

[3] American National Standards Institute, “Synchronous Optical Network (SONET)—Basic Description including Multiplex Structure, Rates, and Formats,” ANSI T1.105-1995, 1995.

[4] Blixt, P., and J. E. Bowers, "An Optical Technique for Bit and Packet Synchronization," IEEE Photonics Technology Letters, **7**, 123, 1995.

[5] Cheng, Y., J. T. Kringlebotn, W. H. Loh, R. I. Laming, and D. N. Payne, “Stable single-frequency traveling-wave fiber loop laser with integral saturable-absorber-based tracking narrow-band filter,” Optics Letters, **20**, 875, 1995.

[6] Chlamtac, I., A. Fumagalli, L. G. Kazovsky, P. Melman, W. H. Nelson, P. Poggiolini, M. Cerisola, A. N. M. M. Choudhury, T. K. Fong, R. T. Hofmeister, C. L. Lu, A. Mekkittikul, D. J. M. Sabido IX, C. J. Suh, and E. W. M. Wong, "CORD: Contention Resolution by Delay Lines," IEEE Journal on Selected Areas in Communications, **14**, 1014, 1996.

[7] Danielsen, S. L., P. B. Hansen, and K. E. Stubkjaer, “Wavelength Conversion in Optical Packet Switching,” IEEE Journal of Lightwave Technology, **16**, 2095, 1998.

[8] Dawson, J. W., N. Park, and K. J. Vahala, “An Improved Delayed Self-Heterodyne Interferometer for Linewidth Measurements,” IEEE Photonics Technology Letters, **4**, 1063, 1992.

[9] Derickson, D., ed., *Fiber Optic Test and Measurement* (Upper Saddle River: Prentice Hall, 1998), 187.

[10] Engström, L., Lund Reports on Atomic Physics, LRAP-232, 1998 (http://kurslab-atom.fysik.lth.se/Lars/Gfit/html/index.html).

[11] Esman, R. D., and K. J. Williams, “Wideband Efficiency Improvement of Fiber Optic Systems by Carrier Subtraction,” IEEE Photonics Technology Letters, **7**, 218, 1995.

[12] Farwell, M. L., W. S. C. Chang, and D. R. Huber, “Increased Linear Dynamic Range by Low Biasing the Mach-Zehnder Modulator,” IEEE Photonics Technology Letters, **5**, 779, 1993.

[13] Feuer, M. D., “Length and Power Dependence of Self-Adjusting Optical Fiber Filters,” IEEE Photonics Technology Letters, **10**, 1587, 1998.

[14] Fischer, B., J. L. Zyskind, J. W. Sulhoff, and D. J. DiGiovanni, “Nonlinear four-wave mixing in erbium-doped fibre amplifiers,” Electronics Letters, **29**, 1858, 1993.

[15] Fischer, B., J. L. Zyskind, J. W. Sulhoff, and D. J. DiGiovanni, “Nonlinear wave mixing and induced gratings in erbium-doped fiber amplifiers,” Optics Letters, **18**, 2108, 1993.

[16] Foord, A. P., P. A. Davies, and P. A. Greenhalgh, “Optical Demultiplexing for Subcarrier Multiplexed Systems,” IEEE Transactions on Microwave Theory and Techniques, **43**, 2324, 1995.

[17] Frisken, S. J., “Transient Bragg reflection gratings in erbium-doped fiber amplifiers,” Optics Letters, **17**, 1776, 1992.

[18] Fuster, J. M., J. Marti, V. Polo, F. Ramos, and J. L. Corral, “Mitigation of dispersion-induced power penalty in millimetre-wave fibre optic links,” Electronics Letters, **34**, 1869, 1998.

[19] Gnauck, A. H., S. K. Korotky, J. J. Veselka, J. Nagel, C. T. Kemmerer, W. J. Minford, and D. T. Moser, “Dispersion Penalty Reduction Using an Optical Modulator with Adjustable Chirp,” IEEE Photonics Technology Letters, **3**, 916, 1991.

[20] Gopalakrishnan, G. K., K. J. Williams, R. P. Moeller, W. K. Burns, and R. D. Esman, “Fibre-optic link architecture for microwave subcarrier transmission and reception,” Electronics Letters, **31**, 1764, 1995.

[21] Havstad, S. A., A. B. Sahin, O. H. Adamczyk, Y. Xie, and A. E. Willner, “Distance-Independent Microwave and Millimeter-Wave Power Fading Compensation using a Phase Diversity Configuration,” IEEE Photonics Technology Letters, **12**, 1052, 2000.

[22] Havstad, S. A., B. Fischer, A. E. Willner, and M. G. Wickham, “Loop-mirror filters based on saturable-gain or -absorber gratings,” Optics Letters, **24**, 1466,1999.

[23] Havstad, S. A., M. G. Wickham, D. G. Heflinger, P. Nachman, and J. C. Brock, “An optically-efficient RF modulator,” Proceedings of the Optical Fiber Communication Conference, paper ThT2, San Diego, CA, 1999.

[24] Havstad, S. A., Y. Xie, A. B. Sahin, Z. Pan, and A. E. Willner, “Delayed Self-Heterodyne Interferometer Measurements of Narrow Linewidth Fiber Lasers,” Proceedings of the Conference on Lasers and Electro-Optics, paper CWK30, San Francisco, CA, 2000.

[25] Horowitz, M., R. Daisy, and B. Fischer, “Filtering behavior of a self-induced three-mirror cavity formed by intracavity wave mixing in a saturable absorber,” Optics Letters, **21**, 299, 1996.

[26] Horowitz, M., R. Daisy, B. Fischer, and J. Zyskind, “Linewidth-narrowing mechanism in lasers by nonlinear wave mixing,” Optics Letters, **19**, 1406, 1994.

[27] Horowitz, M., R. Daisy, B. Fischer, and J. Zyskind, “Narrow-linewidth, singlemode erbium-doped fibre laser with intracavity wave mixing in saturable absorber,” Electronics Letters, **30**, 648, 1994.

[28] Juodawlkis, P. W., J. L. A. Hughes, C. M. Verber, and K. Grimble, "Time alignment of optical cells with arbitrary message payloads," Proceedings of the Optical Fiber Communication Conference, paper WD4, San Jose, CA, 1996.

[29] Karasan, E., and E. Ayanoglu, “Performance of WDM Transport Networks,” IEEE Journal on Selected Areas in Communications, **16**, 1081, 1998.

[30] Kishi, N., and T. Yazaki, “Frequency Control of a Single-Frequency Fiber Laser by Cooperatively Induced Spatial-Hole Burning,” IEEE Photonics Technology Letters, **11**, 182, 1999.

[31] LaGasse, M. J., W. Charczenko, M. C. Hamilton, and S. Thaniyavarn, “Optical carrier filtering for high dynamic range fibre optic links,” Electronics Letters, **30**, 2157, 1994.

[32] Limberger, H. G., and D. Varelas, “Advances in Fiber Gratings: Technology, Applications, and Reliability,” Addendum to SPIE Critical Review Volume CR73, SPIE Press, 1999.

[33] Lu, C. L., D. J. M. Sabido IX, R. T. Hofmeister, P. Poggiolini, and L. G. Kazovsky, "Power budget optimisation of WDM network with MSCM control," Electronics Letters, **31**, 1598, 1995.

[34] Lui, G. L., and H. H. Tan, “Frame Synchronization for Direct-Detection Optical Communication Systems,” IEEE Transactions on Communications, **COM-34**, 227, 1986.

[35] Marti, J., J. M. Fuster, and R. I. Laming, “Experimental reduction of chromatic dispersion effects in lightwave microwave/millimetre-wave transmissions using tapered linearly chirped fibre gratings,” Electronics Letters, **33**, 1170, 1997.

[36] Matsunga, H., and H. Uematsu, “A 1.5 Gb/s 8x8 Cross-Connect Switch Using a Time Reservation Algorithm,” IEEE Journal on Selected Areas in Communications, **9**, 1308, 1991.

[37] Mercer, L. B., “1/f Frequency Noise Effects on Self-Heterodyne Linewidth Measurements,” IEEE Journal of Lightwave Technology, **9**, 485, 1991.

[38] Okoshi, T., K. Kikuchi, and A. Nakayama, “Novel Method for High Resolution Measurement of Laser Output Spectrum,” Electronics Letters, **16**, 630, 1980.

[39] Pan, J. J., Y. Shi, and T. Zhu, “Continuously Tunable High Power Fiber Lasers With 11 nm Tunability," Proceedings of the Optical Fiber Communication Conference, paper WM2, San Diego, CA, 1999.

[40] Park, J., M. S. Shakouri, and K. Y. Lau, “Millimetre-wave electro-optical upconverter for wireless digital communications,” Electronics Letters, **31**, 1085, 1995.

[41] Prucnal, P. R., "Optically Processed Self-Routing, Synchronization, and Contention Resolution for 1-D and 2-D Photonic Switching Architectures," IEEE Journal of Quantum Electronics, **29**, 600, 1993.

[42] Ramos, F., and J. Marti, “Comparison of Optical Single-Sideband Modulation and Chirped Fiber Gratings as Dispersion Mitigating Techniques in Optical Millimeter-Wave Multichannel Systems,” IEEE Photonics Technology Letters, **11**, 1479, 1999.

[43] Renaud, C. C., R. J. Selvas-Aguilar, J. Nilsson, P.W. Turner, and A. B. Grudinin, “Compact High-Energy Q-Switched Cladding-Pumped Fiber Laser with a Tuning Range Over 40 nm,” IEEE Photonics Technology Letters, **11**, 976, 1999.

[44] Richter, L. E., H. I. Mandelberg, M. S. Kruger, and P. A. McGrath, “Linewidth Determination from Self-Heterodyne Measurements with Subcoherence Delay Times,” IEEE Journal of Quantum Electronics, **QE-22**, 2070, 1986.

[45] Sadot, D., and E. Boimovich, “Tunable Optical Filters for Dense WDM Networks,” IEEE Communications Magazine, **36**, 50, 1998.

[46] Saleh, A. A. M., and J. Stone, “Two-Stage Fabry-Perot Filters as Demultiplexers in Optical FDMA LAN’s,” IEEE Journal of Lightwave Technology, **7**, 323, 1989.

[47] Sangsiri, T., S. A. Havstad, C. Kim, X. Jiang, B. Hoanca, and A. E. Willner, “Bit Synchronization Using Subcarriers for Control Signaling,” IEEE Photonics Technology Letters, **11**, 602, 1999.

[48] Schmuck, H., “Comparison of optical millimetre-wave system concepts with regard to chromatic dispersion,” Electronics Letters, **31**, 1848, 1995.

[49] Shieh, W., E. Park, and A. E. Willner, "Demonstration of Output-Port Contention Resolution in a WDM Switching Node Based On All-Optical Wavelength Shifting and Subcarrier-Multiplexed Routing-Control Headers," IEEE Photonics Technology Letters, **9**, 1023, 1997.

[50] Smith, G. H., D. Novak, and Z. Ahmed, “Novel Technique For Generation Of Optical SSB With Carrier Using A Single MZM To Overcome Fiber Chromatic Dispersion,” Proceedings of the International Topical Meeting on Microwave Photonics, paper PDP-2, Kyoto, Japan, 1996.

[51] Song, Y. W., S. A. Havstad, D. Starodubov, Y. Xie, A. E. Willner, and J. Feinberg, “A Single-Mode Erbium-Doped Fiber Ring Laser with 40-nm Tuning Range Using a Stretchable FBG,” Proceedings of Optical Amplifiers and Their Applications, paper OTuD5, Quebec, Canada, 2000.

[52] Starodubov, D. S., V. Grubsky, and J. Feinberg, “Ultrastrong Fiber Gratings and Their Applications,” SPIE Proceedings Volume 3848, SPIE Press, 1999.

[53] Sun, H., M. C. Cardakli, K. M. Feng, J. X. Cai, H. Long, M. I. Hayee, and A. E. Willner, “Tunable RF-Power-Fading Compensation of Multiple-Channel Double-Sideband SCM Transmission Using a Nonlinearly Chirped FBG,” IEEE Photonics Technology Letters, **12**, 546, 2000.

[54] Timofeev, F. N., S. Bennet, R. Griffin, P. Bayvel, A. J. Seeds, R. Wyatt, R. Kashyap, and M. Robertson, "High spectral purity millimetre-wave modulated optical signal generation using fibre grating lasers," Electronics Letters, **34**, 668, 1998.

[55] Tsang, C. S., and W. C. Lindsey, "Bit Synchronization in the Presence of Asymmetric Channel Noise," IEEE Transactions on Communications, **COM-34**, 528, 1986.

[56] Tsukada, M., W. D. Zhong, T. Matsunaga, M. Asobe, and T. Oohara, "An Ultrafast Photonic ATM Switch Based on Bit-Interleave Multiplexing," IEEE Journal of Lightwave Technology, **14**, 1979, 1996.

[57] Wennekers, P., U. Novotny, A. Huelsmann, G. Kaufel, K. Koehler, B. Raynor, and J. Schneider, "10-Gb/s Bit-Synchronizer Circuit with Automatic Timing Alignment by Clock Phase Shifting Using Quantum-Well AlGaAs/GaAs/AlGaAs Technology," IEEE Journal of Solid State Circuits, **27**, 1347, 1992.

[58] Yamashita, S., and M. Nishihara, "Widely Tunable Erbium-Doped Fiber Ring Laser over 80 nm," Proceedings of the Fifth Asia-Pacific Conference on Communications and Fourth Optoelectronics and Communications Conference, paper C6S6, Beijing, China, 1999.